1   # Towards a model for structured mass movements: the

2   # OpenLISEM Hazard model 2.0a

3   Bastian van den Bout*[1] Theo van Asch[2] Wei Hu[2] Chenxiao X. Tang[3] Olga Mavrouli[1] Victor G. Jetten[1] Cees J.
4   van Westen[1]

5   [1]University of Twente, Faculty of Geo-Information Science and Earth Observation

6   [2]Chengdu university of Technology, State key Laboratory of Geohazard Preventaion and GeoEnvironment
7   Protection

8   [3]Institute of Mountain Hazards and Environment, Chinese Academy of Sciences

9   *Correspondence to*: Bastian van den Bout (b.vandenbout@utwente.nl)

10

11   **Abstract**

12   Mass movements such as debris flows and landslide differ in behavior due to their material properties and
13   internal forces. Models employ generalized multi-phase flow equations to adaptively describe these complex
14   flow types. However, models commonly assume unstructured and fragmented flow after initiation of movement.
15   In this work, existing work on two-phase mass movement equations are extended to include a full stress-strain
16   relationship that allows for runout of (semi-) structured fluid-solid masses. The work provides both the three-
17   dimensional equations and depth-averaged simplifications. The equations are implemented in a hybrid Material
18   Point Method (MPM) which allows for efficient simulation of stress-strain relationships on discrete smooth
19   particles. Using this framework, the developed model is compared to several flume experiments of clay blocks
20   impacting fixed obstacles. Here, both final deposit patterns and fractures compare well to simulations.
21   Additionally, numerical tests are performed to showcase the range of dynamical behavior produced by the
22   model. Important processes such as fracturing, fragmentation and fluid release are captured by the model. While
23   this provides an important step towards complete mass movement models, several new opportunities arise such
24   as ground-water flow descriptions and application to fragmenting mass movements and block-slides.

25

Introduction

The earths rock cycle involves sudden release and gravity-driven transport of sloping materials. These mass movements have a significant global impact in financial damage and casualties (Nadim et al., 2006; Kjekstad & Highland, 2009). Understanding the physical principles at work at their initiation and runout phase allows for better mitigation and adaptation to the hazard they induce (Corominas et al., 2014). Many varieties of gravitationally-driven mass movements have been categorized according to their material physical parameters and type of movement. Examples are slides, flows and falls consisting of soil, rocks or debris (Varnes, 1987). Major factors in determining the dynamics of mass movement runout are the composition of the moving material and the forces during initiation and runout. Physically-based models attempt to describe the internal and external forces of all these mass movements in a generalized form (David & Richard, 2011; Pudasaini, 2012; Iverson & George, 2014). This allows these models to be applied to a wide variety of cases, while improving predictive range.

Dynamics of geophysical flows are complex and depend on a variety of forces due to their multi-phase interactions (Hutter et al., 1996). Generally, understanding and prediction of geophysical flows takes place through numerical modelling of the flow. A variety of both one, two and three- dimensional sets of equations exist to describe the advection and forces that determine the dynamics of geophysical flows. Examples that simulated a single mixed material (Rickenmann et al., 2006; O'Brien et al., 2007; Luna et al., 2012; van Asch et al., 2014). Two phase models describe both solids, fluids and their interactions and provide additional detail and generalize in important ways (Sheridan et al., 2005; Pitman & Le, 2005; Pudasaini, 2012;George & Iverson, 2014; Mergili et al., 2017). Recently, a three-phase model has been developed that includes the interactions between small and larger solid phases (Pudasaini & Mergili, 2019). Typically, implemented forces include gravitational forces and, depending on the rheology of the equations, drag forces, viscous internal forces and a plasticity-criterion.

A major assumption made for current models is the a fully mixed and fragmented nature of the material (Iverson & Denlinger 2001; Pudasaini & Hutter, 2003). This assumption is invalid for any structured mass movement. Observations of mass movement types indicate that mixing and fracturing is not a necessary process (Varnes, 1987). Instead, block or slide movement can retain structure during their dynamic stage, as the material is able to resists the internal deformation stresses. Some models do a non-Newtonian viscous yield stress based on depth-averaged strain estimations (Boetticher et al., 2016; Fornes et al., 2017; Pudasaini & Mergili, 2019). However, this approach lacks the process of fragmentation and internal failure. Thus, within current mass movement models, there might be improvements available from assuming non-fragmented movement. This would allow for description of structured mass movement dynamics.

The general importance of the initially structured nature of mass movement material is observed for a variety of reasons. First, block slides are an important subset of mass movement types (Hayir, 2003; Beutner et al., 2008; Tang et al., 2008). This type of mass movement features some cohesive structure to the dynamic material in the movement phase. Secondly, during movement, the spatial gradients in local acceleration induce strain and stress that results in fracturing. This process, often called fragmentation in relation to structured mass movements, can be of crucial importance for mass movement dynamics (Davies & McSaveney, 2009; Delaney & Evans, 2014; Dufresne et al., 2018; Corominas et al. 2019). Lubricating effect from basal fragmentation can enhance velocities and runout distance significantly (Davies et al., 2006;Tang et al., 2009). Otherwise, fragmentation generally influences the rheology of the movement by altering grain-grain interactions (Zhou et al., 2005). The importance of structured material dynamics is further indicated by engineering studies on rock behavior and fracture models (Kaklauskas & Ghaboussi, 2001; Ngekpe et al., 2016; Dhanmeher, 2017)

In this paper, existing two-phase generalized debris flow equations are adapted to describe runout of a arbitrarily structured two-phase Mohr-Coulomb material. The second section of this work provides the derivation of the extensive set of equations that describe structured mass movements in a generalized manner. The third section validates the developed model by comparison with results from controlled flume runout experiments. Additionally, this section shows numerical simulation examples that highlight fragmentation behavior and its influence on runout dynamics. Finally, in section four, a discussion on the potential usage of the presented model is provided together with reflection on important opportunities of improvement.

1. A set of debris flow equations incorporating internal structure

1.1 Structured mass movements

Initiation of gravitational mass flows occurs when sloping material is released. The instability of such materials is generally understood to take place along a failure plane (Zhang et al., 2011, Stead & Wolter, 2015). Along this plane, forces exerted due to gravity and possible seismic accelerations can act as a driving force towards the downslope direction, while a normal-force on the terrain induces a resisting force (Xie et al., 2006).

82 When internal stress exceeds a specified criteria, commonly described using Mohr-Coulomb theory, fracturing
83 occurs, and the material becomes dynamic. Observations indicate material can initially fracture predominantly at
84 the failure plane (Tang et al., 2009 Davies et al., 2006). Full finite-element modelling of stability confirms no
85 fragmentation occurs at initiation, and runout can start as a structured mass (Matsui & San, 1992; Griffiths &
86 Lane, 1999).

87 Once movement is initiated, the material is accelerated. Due to spatially non-homogeneous acceleration,
88 either caused by a non-homogeneous terrain slope, or impact with obstacles, internal stress can build within the
89 moving mass. The stress state can reach a point outside the yield surface, after which some form of deformation
90 occurs (e.g. Plastic, Brittle, ductile) (Loehnert et al., 2008). In the case of rock or soil material, elastic/plastic
91 deformation is limited and fracturing occurs at relatively low strain values (Kaklauskas & Ghaboussi, 2001;
92 Dhanmeher., 2017). Rocks and soil additionally show predominantly brittle fracturing, where strain increments
93 at maximum stress are small (Bieniawaski, 1967; Price, 2016; Husek et al., 2016). For soil matrices, cohesive
94 bonds between grains originate from causes such as cementing, frictionl contacts and root networks (Cohen et
95 al., 2009). Thus, the material breaks along either the grain-grain bonds or on the molecular level. In practice, this
96 processes of fragmentation has been both observed and studied frequently. Cracking models for solids use stress-
97 strain descriptions of continuum mechanics (Menin et al., 2009; Ngekpe et al., 2016). Fracture models frequently
98 use Smooth Particle Hydrodynamics (SPH) since a Lagrangian, meshfree solution benefits possible fracturing
99 behavior (Maurel & Combescure, 2008; Xu et al., 2010; Osorno & Steeb, 2017). Within the model developed
100 below, knowledge from fracture-simulating continuum mechanical models is combined with finite element fluid
101 dynamic models.

102 **1.2 Model description**

103 We define two phases, solids and fluids, within the flow, indicated by s and f respectively. A specified
104 fraction of solids within this mixture is at any point part of a structured matrix. This structured solid phase,
105 indicated by sc envelops and confines a fraction of the fluids in the mixture, indicates as fc. The solids and
106 fluids are defined in terms of the physical properties such as densities (ρ_f, ρ_s) and volume fractions ($\alpha_f =$
107 $\frac{s}{f+s}, \alpha_s = \frac{f}{f+s}$). The confined fractions of their respective phases are indicated as f_{sc} and f_{fc} for the volume
108 fraction of confined solids and fluids respectively (Equations 1,2 and 3).

109   1. $\alpha_s + \alpha_f = 1$

110   2. $\alpha_s\left(f_{sc} + (1 - f_{sc})\right) + \alpha_f\left(f_{fc} + \left(1 - f_{fc}\right)\right) = 1$

111   3. $\left(f_{sc} + (1 - f_{sc})\right) = \left(f_{fc} + \left(1 - f_{fc}\right)\right) = 1$

112 For the solids, additionally internal friction angle (ϕ_s) and effective (volume-averaged) material size
113 (d_s) are defined. We additionally define $\alpha_c = \alpha_s + f_{fc}\alpha_f$ and $\alpha_u = (1 - f_{fc})\alpha_f$ to indicate the solids with
114 confined fluids and free fluid phases respectively. These phases have a volume-averaged density ρ_{sc}, ρ_f. We let
115 the velocities of the unconfined fluid phase ($\alpha_u == (1 - f_{fc})\alpha_f$) be defined as $u_u = (u_u, v_u)$. We assume
116 velocities of the confined phases ($\alpha_c = \alpha_s + f_{fc}\alpha_f$) can validly be assumed to be identical to the velocities of
117 the solid phase, $u_c = (u_c, v_c) = u_s = (u_s, v_s)$. A schematic depiction of the represented phases is shown in
118 Figure 1.
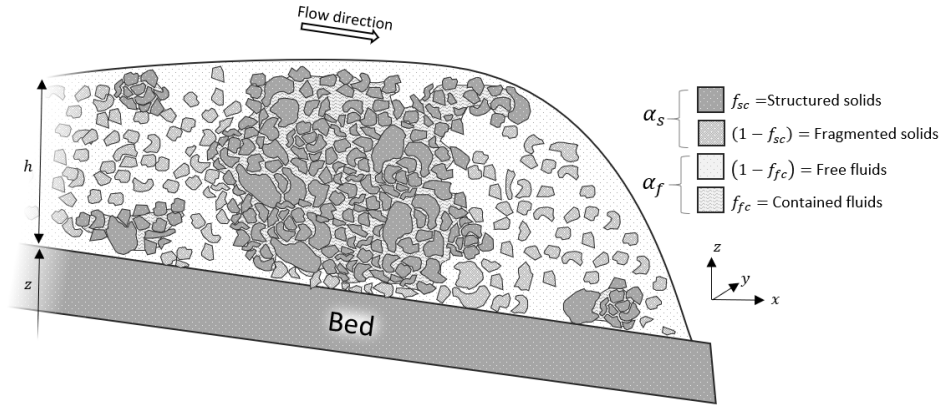
119

120 *Figure 1 A schematic depiction of the flow contents. Both structured and unstructured solids are*
121 *present. Fluids can be either free, or confined by the structured solids.*

122   A major assumption is made here concerning the velocities of both the confined and free solids (sc and
123 s), that have a shared averaged velocity (u_s). We deliberately limit the flow description to two phases, opposed
124 to the innovative work of Pudasaini & Mergili (2019) that develop a multi-mechanical three-phase model. This
125 choice is motivated by considerations of applicability (reducing the number of required parameters), the infancy
126 of three-phase flow descriptions and finally the general observations of the validity of this assumption (Ishii,
127 1975; Ishii & Zuber, 1979; Drew, 1983; Jakob et al, 2005; George & Iverson, 2016).

128   The movement of the flow is described initially by means of mass and momentum conservation
129 (Equations 4 and 5).

130   4. $\frac{\partial \alpha_c}{\partial t} + \nabla \cdot (\alpha_c \boldsymbol{u}_c) = 0$

131   5. $\frac{\partial \alpha_u}{\partial t} + \nabla \cdot (\alpha_u \boldsymbol{u}_u) = 0$

132   Here we add the individual forces based on the work of Pudasaini & Hutter (2003), Pitman & Le
133 (2005), Pudasaini (2012), Pudasaini & Fischer (2016) and Pudasaini & Mergili (2019) (Equations 6 and 7).

134   6. $\frac{\partial}{\partial t}(\alpha_c \rho_c \boldsymbol{u}_c) + \nabla \cdot (\alpha_c \rho_c \boldsymbol{u}_c \otimes \boldsymbol{u}_c) = \alpha_c \rho_c \boldsymbol{f} - \nabla \cdot \alpha_c \boldsymbol{T}_c + p_c \nabla \alpha_c + \boldsymbol{M}_{DG} + \boldsymbol{M}_{vm}$

135   7. $\frac{\partial}{\partial t}(\alpha_u \rho_f \boldsymbol{u}_u) + \nabla \cdot (\alpha_u \rho_f \boldsymbol{u}_u \otimes \boldsymbol{u}_u) = \alpha_u \rho_f \boldsymbol{f} - \nabla \cdot \alpha_u \boldsymbol{T}_u + p_f \nabla \alpha_u - \boldsymbol{M}_{DG} - \boldsymbol{M}_{vm}$

136   Where $\boldsymbol{f}$ is the body force (among which is gravity), $\boldsymbol{M}_{DG}$ is the drag force, $\boldsymbol{M}_{vm}$ is the virtual mass
137 force and $\boldsymbol{T}_c, \boldsymbol{T}_u$ are the stress tensors for solids with confined fluids and unconfined phases respectively. The
138 virtual mass force described the additional work required by differential acceleration of the phases. The drag
139 force describes the drag along the interfacial boundary of fluids and solids. The body force describes external
140 forces such as gravitational acceleration and boundary forces. Finally, the stress tensors describe the internal
141 forces arising from strain and viscous processes. Both the confined and unconfined phases in the mixture are
142 subject to stress tensors (T_c, and T_u), for which the gradient acts as a momentum source. Additionally, we follow
143 Pudasaini (2012) and add a buoyancy force ($p_c \nabla \alpha_c$ and $p_f \nabla \alpha_u$).

144   **Stress Tensors, Describing internal structure**

145   Based on known two-phase mixture theory, the internal and external forces acting on the moving
146 material are now set up. This results in several unknowns such as the stress tensors ($\boldsymbol{T}_c$ and $\boldsymbol{T}_u$, described by the
147 constitutive equation), the body force ($\boldsymbol{f}$), the drag force ($\boldsymbol{M}_{DG}$) and the virtual mass force ($\boldsymbol{M}_{VM}$). This section
148 will first describe the derivation of the stress tensors. These describe the internal stress and viscous effects. To
149 describe structured movements, these require a full stress-strain relationship which is not present in earlier
150 generalized mass movements model. Afterwards, existing derivation of the body, drag and virtual mass force are
151 altered to conform the new constitutive equation.

152   Our first step in defining the momentum source terms in equations 6 and 7 is the definition of the fluid
153 and solid stress tensors. Current models typically follow the assumptions made by Pitman & Le (2005), who
154 indicate: "*Proportionality and alignment of the tangential and normal forces are imposed as a basal boundary*

155 *condition is assumed to hold throughout the layer of flowing material ... following Rankine (1857) and Terzaghi*
156 *(1936), an earth pressure relation is assumed for diagonal stress components*". Here, the earth pressure
157 relationship is a vertically-averaged analytical solution for lateral forces exerted by an earth wall. Thus,
158 unstructured columns of moving mixtures are assumed. Here, we aim to use the full Mohr-Coulomb relations.
159 Describing the internal tress of soil and rock matrices is commonly achieved be elastic-plastic simulations of the
160 materials stress-strain relationship. Since we aim to model a full stress description, the stress tensor is equal to
161 the elasto-plastic stress tensor (Equation 8).

162   8. $T_c = \boldsymbol{\sigma}$

163   Where $\boldsymbol{\sigma}$ is the elasto-plastic stress tensor for solids. The stress can be divided into the deviatoric and
164 non-deviatoric contributions (Equation 9). The non-deviatoric part acts normal on any plane element (in the
165 manner in which a hydrostatic pressure acts equal in all directions). Note that we switch to tensor notation when
166 describing the stress-strain relationship. Thus, superscripts (α and β) represent the indices of basis vectors (x, y
167 or z axis in Euclidian space), and obtain tensor elements. Additionally, the Einstein convention is followed
168 (automatic summation of non-defined repeated indices in a single term).

169   9. $\sigma^{\alpha\beta} = s^{\alpha\beta} + \frac{1}{3}\sigma^{\gamma\gamma}\delta^{\alpha\beta}$

170   Where s is the deviatoric stress tensor and $\delta^{\alpha\beta} = [\alpha = \beta]$ is the Kronecker delta.

171   Here, we define the elasto-plastic stress (σ) based on a generalized Hooke-type law in tensor notation
172 (Equation 10 and 11) where plastic strain occurs when the stress state reaches the yield criterion (Spencer, 2004;
173 Necas & Hiavecek, 2007; Bui et al., 2008).

174   10. $\dot{\epsilon}^{\alpha\beta}_{elastic} = \frac{\dot{s}^{\alpha\beta}}{2G} + \frac{1-2\nu}{E}\dot{\sigma}^m\delta^{\alpha\beta}$
175   11. $\dot{\epsilon}^{\alpha\beta}_{plastic} = \dot{\lambda}\frac{\partial g}{\partial \sigma^{\alpha\beta}}$

176   Where $\dot{\epsilon}_{elastic}$ is the elastic strain tensor, $\dot{\epsilon}_{plastic}$ is the plastic strain tensor, $\dot{\sigma}^m$ is the mean stress rate
177 tensor, ν is Poisson's ratio, E is the elastic Young's Modulus, G is the shear modulus, $\dot{s}$ is the deviatoric shear
178 stress rate tensor, $\dot{\lambda}$ is the plastic multiplier rate and g is the plastic potential function. Additionally, the strain
179 rate is defined from velocity gradients as equation 12.

180   12. $\dot{\epsilon}^{\alpha\beta}_{total} = \dot{\epsilon}^{\alpha\beta}_{elastic} + \dot{\epsilon}^{\alpha\beta}_{plastic} = \frac{1}{2}\left(\frac{\partial u_c^\alpha}{\partial x^\beta} - \frac{\partial u_c^\beta}{\partial x^\alpha}\right)$

181   By solving equations 9, 10 and 11 for $\dot{\sigma}$, a stress-strain relationship can be obtained (Equation 13) (Bui
182 et al., 2008).

183   13. $\dot{\sigma}^{\alpha\beta} = 2G\dot{e}^{\gamma\gamma}\delta^{\alpha\beta} + K\dot{\epsilon}^{\gamma\gamma}\delta^{\alpha\beta} - \dot{\lambda}\left[\left(K - \frac{2G}{3}\right)\frac{\partial g}{\partial \sigma^{mn}}\delta^{mn}\delta^{\alpha\beta} + 2G\frac{\partial g}{\partial \sigma^{\alpha\beta}}\right]$

184   Where $\dot{e}$ is the deviatoric strain rate ($\dot{e}^{\alpha\beta} = \dot{\epsilon}^{\gamma\gamma} - \frac{1}{3}\dot{\epsilon}^{\alpha\beta}\delta^{\alpha\beta}$), ψ is the dilatancy angle and K is the
185 elastic bulk modulus and the material parameters defined from from E and ν (Equation 14).

186   14. $K = \frac{E}{3(1-2\nu)}, \quad G = \frac{E}{2(1+\nu)}$

187   Fracturing or failure occurs when the stress state reaches the yield surface, after which plastic
188 deformation occurs. The rate of change of the plastic multiplier specifies the magnitude of plastic loading and
189 must ensure a new stress state conforms to the conditions of the yield criterion. By means of substituting
190 equation 13 in the consistency condition ($\frac{\partial f}{\partial \sigma^{\alpha\beta}}d\sigma^{\alpha\beta} = 0$), the plastic multiplier rate can be defined (Equation
191 15) (Bui et al., 2008).

192   15. $\dot{\lambda} = \frac{2G\epsilon^{\alpha\beta}\frac{\partial f}{\partial \sigma^{\alpha\beta}} + \left(K - \frac{2G}{3}\right)\dot{\epsilon}^{\gamma\gamma}\frac{\partial f}{\partial \sigma^{\alpha\beta}}\sigma^{\alpha\beta}\delta^{\alpha\beta}}{2G\frac{\partial f}{\partial \sigma^{mn}}\frac{\partial g}{\partial \sigma^{mn}} + \left(K - \frac{2G}{3}\right)\frac{\partial f}{\partial \sigma^{mn}}\delta^{mn}\frac{\partial g}{\partial \sigma^{mn}}\delta^{mn}}$

193   The yield criteria specifies a surface in the stress-state space that the stress state can not pass, and at
194 which plastic deformation occurs. A variety of yield criteria exist, such as Mohr-Coulomb, Von Mises, Ducker-
195 Prager and Tresca (Spencer, 2004). Here, we employ the Ducker-Prager model fitted to Mohr-Coulomb material
196 parameters for its accuracy in simulating rock and soil behavior, and numerical stability (Spencer, 2004; Bui et
197 al., 2008) (Equation 16 and 17).

198   16. $f(I_1, J_2) = \sqrt{J_2} + \alpha_\phi I_1 - k_c = 0$
199   17. $g(I_1, J_2) = \sqrt{J_2} + \alpha_\phi I_1 \sin(\psi)$

200   Where I_1 and J_2 are tensor invariants (Equation 18 and 19).

201   18. $I_1 = \sigma^{xx} + \sigma^{yy} + \sigma^{zz}$

202   19. $J_2 = \frac{1}{2} s^{\alpha\beta} s^{\alpha\beta}$

203   Where the Mohr-Coulomb material parameters are used to estimate the Ducker-Prager parameters
204   (Equation 20).

205   20. $\alpha_\phi = \frac{\tan(\phi)}{\sqrt{9 + 12\tan^2\phi}}, \quad k_c = \frac{3c}{\sqrt{9 + 12\tan^2\phi}}$

206   Using the definitions of the yield surface and stress-strain relationship, combining equations 13, 15, 16
207   and 17, the relationship for the stress rate can be obtained (Equation 21 and 22).

208   21. $\dot{\sigma} = 2G\dot{e}^{\alpha\beta} + K\dot{\epsilon}^{\gamma\gamma}\delta^{\alpha\beta} - \dot{\lambda}\left[9K\sin\psi\,\delta^{\alpha\beta} + \frac{G}{\sqrt{J_2}} s^{\alpha\beta}\right]$

209   22. $\dot{\lambda} = \frac{3\alpha K\dot{\epsilon}^{\gamma\gamma} + \left(\frac{G}{\sqrt{J_2}}\right) s^{\alpha\beta}\dot{\epsilon}^{\alpha\beta}}{27\alpha_\phi K\sin\psi + G}$

210   In order to allow for the description of large deformation, the Joumann stress rate can be used, which is
211   a stress-rate that is independent from a frame of reference (Equation 23).

212   23. $\hat{\sigma} = \sigma^{\alpha\gamma}\dot{\omega}^{\beta\gamma} + \sigma^{\gamma\beta}\dot{\omega}^{\alpha\gamma} + 2G\dot{e}^{\alpha\beta} + K\dot{\epsilon}^{\gamma\gamma}\delta^{\alpha\beta} - \dot{\lambda}\left[9K\sin\psi\,\delta^{\alpha\beta} + \frac{G}{\sqrt{J_2}} s^{\alpha\beta}\right]$

213   Where $\dot{\omega}$ is the spin rate tensor, as defined by equation 24.

214   24. $\dot{\omega}^{\alpha\beta} = \frac{1}{2}\left(\frac{\partial v^\alpha}{\partial x^\beta} - \frac{\partial v^\beta}{\partial x^\alpha}\right)$

215   Due to the strain within the confined material, the density of the confined solid phase (ρ_c) evolves
216   dynamically according to equation 25.

217   25. $\rho_c = f_{sc}\rho_s \frac{\epsilon_{v0}}{\epsilon_v} + (1 - f_{sc})\rho_s + f_{fc}\rho_f$

218   Where ϵ_v is the total volume strain, $\epsilon_v \approx \epsilon_1 + \epsilon_2 + \epsilon_3$, ϵ_i is one of the principal components of the
219   strain tensor. Since we aim to simulate brittle materials, where volume strain remains relatively low, we assume
220   that changes in density are small compared to the original density of the material ($\frac{\partial \rho_c}{\partial t} \ll \rho_c$).

221   **Fragmentation**

222   Brittle fracturing is a processes commonly understood to take place once a material internal stress has
223   reached the yield surface, and plastic deformation has been sufficient to pass the ultimate strength point (Maurel
224   & Cumescure, 2008; Husek et al., 2016). A variety of approaches to fracturing exist within the literature (Ma et
225   al., 2014; Osomo & Steeb, 2017). FEM models use strain-based approaches (Loehnert et al., 2008). For SPH
226   implementations, as will be presented in this work, distance-based approaches have provided good results
227   (Maurel & Cumbescure, 2008). Other works have used strain-based fracture criteria (Xu et al., 2010) .
228   Additionally, dynamic degradation of strength parameters have been implemented (Grady & Kipp, 1980; Vuyst
229   & Vignjevic, 2013; Williams, 2019). Comparisons with observed fracture behavior has indicated the predictive
230   value of these schemes (Xu et al., 2010; Husek et al., 2016). We combine the various approaches to best fit the
231   dynamical multi-phase mass movement model that is developed. Following, Grady & Kipp (1980) and we
232   simulate a degradation of strength parameters. Our material consists of a soil and rock matrix. We assume
233   fracturing occurs along the inter-granular or inter-rock contacts and bonds (see also Cohen et al., 2009). Thus,
234   cohesive strength is lost for any fractured contacts. We simulate degradation of cohesive strength according to a
235   volume strain criteria. When the stress state lies on the yield surface (the set of critical stress states within the 6-
236   dimensional stress-space), during plastic deformation, strain is assumed to attribute towards fracturing. A critical
237   volume strain is taken as material property, and the breaking of cohesive bonds occurs based on the relative
238   volume strain. Following Grady & Kipp (1980) and Vuyst & Vignjevic (2013), we assume that the degradation
239   behavior of the strength parameter is distributed according to a probability density distribution. Commonly, a
240   Weibull-distribution is used (Williams, 2019). Here, for simplicity, we use a uniform distribution of cohesive
241   strength between 0 and $2c_0$, although any other distribution can be substituted. Thus, the expression governing
242   cohesive strength becomes equation 26

243   26. $\frac{\partial c}{\partial t} = \begin{cases} -c_0 \frac{1}{2} \frac{\left(\frac{\epsilon_v}{\epsilon_{v0}}\right)}{\epsilon_c} & f(I_1, J_2) \geq 0, c > 0 \\ 0 & otherwise \end{cases}$

244   Where c_0 is the initial cohesive strength of the material, ϵ_{v0} is the initial volume, $\left(\frac{\epsilon_v}{\epsilon_{v0}}\right)$ is the fractional
245   volumetric strain rate, ϵ_c is the critical fractional volume strain for fracturing.

Water partitioning

247   During the movement of the mixed mass, the solids can thus be present as a structured matrix. Within
248   such a matrix, a fluid volume can be contained (e.g. as originating from a ground water content in the original
249   landslide material). These fluids are typically described as groundwater flow following Darcy's law, which poses
250   a linear relationship between pressure gradients and flow velocity through a soil matrix. In our case, we assumed
251   the relative velocity of water flow within the granular solid matrix as very small compared to both solid
252   velocities and the velocities of the free fluids. As an initial condition of the material, some fraction of the water
253   is contained within the soil matrix (f_{fc}). Additionally, for loss of cohesive structure within the solid phase, we
254   transfer the related fraction of fluids contained within that solid structure to the free fluids.

255   27. $\dfrac{\partial f_{fc}}{\partial t} = -\dfrac{\partial (1-f_{fc})}{\partial t} = \begin{cases} -f_{fc}\dfrac{c_0}{c}\dfrac{\max(0.0,\epsilon_v)}{\epsilon_f} & f(I_1,J_2) \geq 0, c > 0 \\ 0 & otherwise \end{cases}$

256   28. $\dfrac{\partial f_{sc}}{\partial t} = -\dfrac{\partial (1-f_{sc})}{\partial t} = \begin{cases} -f_{sc}\dfrac{c_0}{c}\dfrac{\max(0.0,\epsilon_v)}{\epsilon_f} & f(I_1,J_2) \geq 0, c > 0 \\ 0 & otherwise \end{cases}$

257   Beyond changes in f_{fc} through fracturing of structured solid materials, no dynamics are simulated for
258   in- or outflux of fluids from the solid-matrix. The initial volume fraction of fluids in the solid matrix defined by
259   ($f f_{fc}$ and $s f_{sc}$) remains constant throughout the simulation. The validity of this assumption can be based on the
260   slow typical fluid velocities in a solid matrix relative to fragmented mixed fluid-solid flow velocities (Kern,
261   1995; Saxton and Rawls, 2006). While the addition of evolving saturation would extend validity of the model, it
262   would require implementation of pretransfer-functions for evolving material properties, which is beyond the
263   scope of this work. An important note on the points made above is the manner in which fluids are re-partitioned
264   after fragmentation. All fluids in fragmented solids are released, but this does not equate to free movement of the
265   fluids or a disconnection from the solids that confined them. Instead, the equations continue to connect the solids
266   and fluids through drag, viscous and virtual mass forces. Finally, the density of the fragmented solids is assumed
267   to be the initially set solid density. Any strain-induced density changes are assumed small relative to the initial
268   solid density ($\frac{\rho_c}{\rho_s} \ll 1$).

Fluid Stresses

270   The fluid stress tensor is determined by the pressure and the viscous terms (Equations 29 and 30).
271   Confined solids are assumed to be saturated and constant during the flow.

272   29. $\boldsymbol{T}_u = P_f \boldsymbol{I} + \boldsymbol{\tau}_f$
273   30. $\boldsymbol{\tau}_f = \eta_f[\nabla \boldsymbol{u}_u + (\nabla \boldsymbol{u}_c)^t] - \dfrac{\eta_f}{\alpha_u}\mathcal{A}(\alpha_u)(\nabla\alpha_c(\boldsymbol{u}_u - \boldsymbol{u}_c) + (\boldsymbol{u}_c - \boldsymbol{u}_u)\nabla\alpha_c)$

274   Where $\boldsymbol{I}$ is the identity tensor, $\boldsymbol{\tau}_f$ is the viscous stress tensor for fluids , P_f is the fluid pressure, η_f is the
275   dynamic viscosity of the fluids and $\mathcal{A}$ is the mobility of the fluids at the interface with the solids that acts as a
276   phenomenological parameter (Pudasaini, 2012).

277   The fluid pressure acts only on the free fluids here, as the confined fluids are moved together with the
278   solids. In equation 30, the second term is related to the non-Newtonian viscous force induced by gradients in
279   solid concentration. The effect as described by Pudasaini (2012) is induced by a solid-concentration gradient. In
280   case of unconfined fluids and unstructured solids ($f_{sf} = 1, f_{sf} = 1$). Within our flow description, we see no
281   direct reason to eliminate or alter this force with a variation in the fraction of confined fluids or structured solids.
282   We do only consider the interface between solids and free fluids as an agent that induces this effect, and
283   therefore the gradient of the gradient of the solids and confined fluids ($\nabla(\alpha_s + f_{fc}\alpha_f) = \nabla\alpha_c$) is used instead of
284   the total solid phase ($\nabla\alpha_s$).

Drag force and Virtual Mass

286   Our description of the drag force follows the work of Pudasaini (2012) and Pudasaini (2018), where a
287   generalized two-phase drag model is introduced and enhanced. We split their work into a contribution from the
288   fraction of structured solids (f_{sc}) and unconfined fluids ($1 - f_{fc}$) (Equation 31).

289   31. $\mathcal{C}_{DG} = \dfrac{f_{sc}\alpha_c\alpha_u(\rho_c-\rho_f)g}{U_{T,c}(\mathcal{G}(Re))+S_p}(\boldsymbol{u}_u - \boldsymbol{u}_c)|\boldsymbol{u}_u - \boldsymbol{u}_c|^{j-1} + \dfrac{(1-f_{sc})\alpha_c\alpha_u(\rho_s-\rho_f)g}{U_{T,uc}(\mathcal{PF}(Re_p)+(1-\mathcal{P})\mathcal{G}(Re))+S_p}(\boldsymbol{u}_u - \boldsymbol{u}_c)|\boldsymbol{u}_u - \boldsymbol{u}_c|^{j-1}$

290   Where $U_{T,c}$ is the terminal or settling velocity of the structures solids, $U_{T,uc}$ is the terminal velocity of
291   the unconfined solids, $\mathcal{P}$ is a factor that combines solid- and fluid like contributions to the drag force, $\mathcal{G}$ is the
292   solid-like drag contribution, $\mathcal{F}$ is the fluid-like drag contribution and S_p is the smoothing function (Equation 32
293   and 34). The exponent j indicates the type of drag: linear ($j = 0$) or quadratic ($j = 1$).

294   Within the drag, the following functions are defined:

295   32. $F = \frac{\gamma}{180} \left(\frac{\alpha_f}{\alpha_s}\right)^3 Re_P, \ G = \alpha_f^{M(Re_p)-1}$

296   33. $S_p = \left(\frac{\mathcal{P}}{\alpha_c} + \frac{1-\mathcal{P}}{\alpha_u}\right)\mathcal{K}$

297   34. $\mathcal{K} = |\alpha_c \boldsymbol{u}_c + \alpha_u \boldsymbol{u}_u| \approx 10 \ ms^{-1}$

298   Where M is a parameter that varies between 2.4 and 4.65 based on the Reynolds number (Pitman & Le,
299   2005). The factor $\mathcal{P}$ that combines solid-and fluid like contributions to the drag, is dependent on the volumetric
300   solid content in the unconfined and unstructured materials ($\mathcal{P} = \left(\frac{\alpha_s(1-f_{sc})}{\alpha_f(1-f_{fc})}\right)^m$ with $m \approx 1$. Additionally we
301   assume the factor $\mathcal{P}$, is zero for drag originating from the structured solids. As stated by Pudasaini & Mergili
302   (2019) "As limiting cases: $\mathcal{P}$ suitably models solid particles moving through a fluid". In our model, the drag
303   force acts on the unconfined fluid momentum ($u_{uc}\alpha_f(1 - f_{fc})$). For interactions between unconfined fluids and
304   structured solids, larger blocks of solid structures are moving through fluids that contains solids of smaller size.

305   Virtual mass is similarly implemented based on the work of Pudasaini (2012) and Pudasaini & Mergili
306   (2019) (Equation 35). The adapted implementation considers the solids together with confined fluids to move
307   through a free fluid phase.

308   35. $\mathcal{C}_{VMG} = \alpha_c \rho_u \left(\frac{1}{2}\left(\frac{1+2\alpha_c}{\alpha_u}\right)\right)\left(\left(\frac{\partial u_u}{\partial t} + u_u \cdot \nabla u_u\right) - \left(\frac{\partial u_c}{\partial t} + u_c \cdot \nabla u_c\right)\right)$

309   Where $C_{DG} = \frac{1}{2}\left(\frac{1+2\alpha_c}{\alpha_u}\right)$ is the drag coefficient.

310   boundary conditions

311   Finally, following the work of Iverson & Denlinger (2001), Pitman & Le (2005) and Pudasaini (2012), a
312   boundary condition is applied to the surface elements that contact the flow (Equation 36).

313   36. $|\boldsymbol{S}| = Ntan(\phi)$

314   Where N is the normal pressure on the surface element and $\boldsymbol{S}$ is the shear stress.

315   1.3 Depth-Averaging

316   The majority of the depth-averaging in this works is analogous to the work of Pitman & Le (2005),
317   Pudasaini (2012) and Pudasini & Mergili (2019). Depth-averaging through integration over the vertical extent of
318   the flow can be done based on several useful and often-used assumptions: $\frac{1}{h}\int_0^h x \, dh = \bar{x}$, for the velocities ($u_u$
319   and u_c), solid, fluid and confined fractions ($\alpha_f, \alpha_s, f_{fc}$ and f_{sc}) and material properties (ρ_u, ϕ and c). Besides
320   these similarities and an identical derivation of depth-averaged continuity equations, three major differences
321   arise.

322   i)Fluid pressure

323   Previous implementations of generalized two-phase debris flow equations have commonly assumed hydrostatic
324   pressure ($\frac{\partial p}{\partial z} = g^z$) (Pitman & Le, 2005; Pudasaini, 2012; Abe & Konagai, 2016). Here we follow this
325   assumption for the fluid pressure at the base and solid pressure for unstructured material (Equations 37 and 38).

326   37. $P_{b_{s,u}} = -(1 - \gamma)\alpha_s g^z h$

327   38. $P_{b_u} = -g^z h$

328   Where $\gamma = \frac{\rho_f}{\rho_s}$ is the density ratio (not to be confused with a tensor index when used in superscript) (-).

329   However, larger blocks of structure material can have contact with the basal topography. Due to density
330   differences, larger blocks of solid structures are likely to move along the base (Pailhia & Pouliquen, 2009;
331   George & Iverson, 2014). If these blocks are saturated, water pressure propagates through the solid matrix and
332   hydrostatic pressure is retained. However, in cases of an unsaturated solid matrix that connects to the base,
333   hydrostatic pressure is not present there. We introduce a basal fluid pressure propagation factor $\mathcal{B}(\theta_{eff}, \overline{d_{sc}}, ..)$
334   which describes the fraction of fluid pressure propagated through a solid matrix (with θ_{eff} the effective

335 saturation, $\overline{d_{sc}}$ the average size of structured solid matrix blocks). This results in a basal pressure equal to
336 equation 39.

337   39. $P_{b_c} = -(1-f_{sc})(1-\gamma)\frac{(1-f_{sc})\alpha_s}{(1-f_{fc})\alpha_f} g^z h - f_{sc}(1-\gamma)\mathcal{B}\frac{(f_{sc})\alpha_s}{(f_{fc})\alpha_f} g^z h$

338   The basal pressure propagation factor ($\mathcal{B}$) should theoretically depend, similarly to the pedotransfer
339 function, mostly on saturation level, as a full saturation means perfect propagation of pressure through the
340 mixture, and low saturation equates to minimal pressure propagation (Saxton and Rawls., 2006). Additionally it
341 should depend on pedotransfer functions, and the size distribution of structured solid matrices within the
342 mixture. For low-saturation levels, it can be assumed no fluid pressure is retained. Combined with an assumed
343 soil matrix height identical to the total mixture height, this results in $\mathcal{B} = 0$. Assuming saturation of structures
344 solids results in a full propagation of pressures and $\mathcal{B} = 1$.

345   **ii)Stress-Strain relationship**

346   Depth-averaging the stress-strain relationship in equations 22 and 23 requires a vertical solution for the
347 internal stress. First, we assume any non-normal vertical terms are zero (Equation 40). Commonly, Rankines
348 earth pressure coefficients are used to express the lateral earth pressure by assuming vertical stress to be induced
349 by the basal solid pressure (Equation 41 and 42) (Pitman & Le, 2005; Pudasaini, 2012; Abe & Konagai, 2016).

350   40. $\sigma^{zx} = \sigma^{zy} = \sigma^{yz} = \sigma^{xz} = 0$
351   41. $\overline{\sigma^{zz}} = \frac{1}{2}P_{b_s}, \sigma^{zz}|_b = P_{b_s}$
352   42. $K_a = \frac{1-\sin(\phi)}{1+\sin(\phi)}, \quad K_p = \frac{1-\sin(\phi)}{1+\sin(\phi)}$

353   Here we enhance this with Bell's extension for cohesive soils (Equation 45) (Richard et al., 2017). This
354 lateral normal-directed stress term is added to the full stress-strain solution.

355   43. $\overline{\sigma_{xx}} = K\sigma_{zz}|_b - 2c\sqrt{K} + \frac{1}{h}\int_0^h \sigma_{xx}\, dh$

356   Finally, the gradient in pressure of the lateral interfaces between the mixture is added as a depth-
357 averaged acceleration term (Equation 44).

358   44. $S_{x_c} = \alpha_c\left(\frac{1}{h}\left(\frac{\partial(h\sigma^{xx})}{\partial x} + \frac{\partial(h\sigma^{yx})}{\partial y}\right)\right) + \cdots$

359   **iii)Depth-averaging other terms**

360   While the majority of terms allow for depth-averaging as proposed by Pudasaini (2012), an exception
361 arises. Depth-averaging of the vertical viscosity terms is required. The non-Newtonian viscous terms for the fluid
362 phase were derived assuming a vertical profile in the volumetric solid phase content. Here, we alter the
363 derivation to use this assumption only for the non-structured solids, as opposed to the structured solids where
364 $\frac{\partial \alpha_s}{\partial z} = 0$.

365   45. $\int_b^s \frac{\partial}{\partial z}\left(\frac{\partial \alpha_s}{\partial z}(u_u - u_c)\right) dz = \left[\frac{\partial \alpha_s}{\partial z}(u_u - u_c)\right]_b^s = (\overline{u_u} - \overline{u_c})\left[\frac{\partial \alpha_s}{\partial z}\right]_b^s = (\overline{u_u} - \overline{u_c})\left[\frac{\partial \alpha_s}{\partial z}\right]_b^s =$
366      $\frac{(\overline{u_u}-\overline{u_c})(1-f_{sc})\zeta\,\overline{\alpha_s}}{h}$

367   Where ζ is the shape factor for the vertical distribution of solids (Pudasaini, 2012). Additionally, the
368 momentum balance of Pudasaini (2012) ignores any deviatoric stress ($\tau_{xy} = 0$), following Savage and Hutter
369 (2007), and Pudasaini and Hutter (2007). Earlier this term was included by Iverson and Denlinger (2001), Pitman
370 and Le (2005) and Abe &Kanogai (2016). Here we include these terms since a full stress-strain relationship is
371 included.

372 **Basal frictions**
373   Additionally we add the Darcy-Weisbach friction, which is a Chezy-type friction law for the fluid phase
374 that provides drag (Delestre et al., 2014). This ensures that, without solid phase, a clear fluid does lose
375 momentum due to friction from basal shear. This was successfully done in Bout et al. (2018) and was similarly
376 assumed in Pudasaini and Fischer (2016) for fluid basal shear stress.

377   46. $S_f = \frac{g}{n^2}\frac{\mathbf{u_u}|\mathbf{u_u}|}{h^{\frac{4}{3}}}$

378   Where n is Manning's surface roughness coefficient.

379   **Depth-averaged equations**

The following set of equations is thus finally achieved for depth-averaged flow over sloping terrain (Equations 47-71).

47. $\frac{\partial h}{\partial t} + \frac{\partial}{\partial x}[h(\alpha_u u_u + \alpha_c u_c)] + \frac{\partial}{\partial y}[h(\alpha_u u_u + \alpha_c u_c)] = R - I$

48. $\frac{\partial \alpha_c h}{\partial t} + \frac{\partial \alpha_c h u_c}{\partial x} + \frac{\partial \alpha_c h v_c}{\partial y} = 0$

49. $\frac{\partial \alpha_u h}{\partial t} + \frac{\partial \alpha_u h u_u}{\partial x} + \frac{\partial \alpha_u h v_u}{\partial y} = R - I$

50. $\frac{\partial}{\partial t}[\alpha_c h(u_c - \gamma_c C_{VM}(u_u - u_c))] + \frac{\partial}{\partial x}[\alpha_c h(u_c^2 - \gamma_c C_{VM}(u_u^2 - u_c^2))] + \frac{\partial}{\partial y}[\alpha_c h(u_c v_c - \gamma C(u_u v_u - u_c v_c))] = h S_{x_c}$

51. $\frac{\partial}{\partial t}[\alpha_c h(v_c - \gamma_c C_{VM}(v_u - v_c))] + \frac{\partial}{\partial x}[\alpha_c h(u_s v_s - \gamma_c C_{VM}(u_u v_u - u_c v_c))] + \frac{\partial}{\partial y}[\alpha_c h(v_c^2 - \gamma C_{VM}(v_u^2 - v_c^2))] = h S_{y_c}$

52. $\frac{\partial}{\partial t}[\alpha_u h(u_u - \frac{\alpha_c}{\alpha_u} C_{VM}(u_u - u_c))] + \frac{\partial}{\partial x}[\alpha_u h(u_u^2 - \frac{\alpha_c}{\alpha_u} C_{VM}(u_u^2 - u_c^2) + \frac{\beta_{x_u} h}{2})] + \frac{\partial}{\partial y}[\alpha_u h(u_u v_u - \gamma_c C_{VM}(u_u v_u - u_c v_c))] = h S_{x_u} - I u_u$

53. $\frac{\partial}{\partial t}[\alpha_u h(v_u - \frac{\alpha_c}{\alpha_u} C_{VM}(v_u - v_c))] + \frac{\partial}{\partial x}[\alpha_u h(u_u v_u - \frac{\alpha_c}{\alpha_u} C_{VM}(u_u v_u - u_c v_c))] + \frac{\partial}{\partial y}[\alpha_u h(v_u^2 - \gamma_c C_{Vm}(v_u^2 - v_c^2) + \frac{\beta_{y_u} h}{2})] = h S_{y_u} - I v_u$

54. $S_{x_c} = \alpha_c[g^x + \frac{1}{h}(\frac{\partial(h\sigma^{xx})}{\partial x} + \frac{\partial(h\sigma^{yx})}{\partial y}) - P_{b_c}(\frac{u_c}{|\overrightarrow{u_c}|}\tan\phi + \epsilon\frac{\partial b}{\partial x})] - \epsilon\alpha_c\gamma_c p_{b_u}[\frac{\partial h}{\partial x} + \frac{\partial b}{\partial x}] + C_{DG}(u_u - u_c)|\boldsymbol{u}_u - \boldsymbol{u}_c|^{J-1}$

55. $S_{y_c} = \alpha_c[g^y + \frac{1}{h}(\frac{\partial(h\sigma^{xy})}{\partial x} + \frac{\partial(h\sigma^{yy})}{\partial y}) - P_{b_c}(\frac{v_s}{|\overrightarrow{u_s}|}\tan\phi + \epsilon\frac{\partial b}{\partial y})] - \epsilon\alpha_c\gamma_c p_{b_u}[\frac{\partial h}{\partial y} + \frac{\partial b}{\partial y}] + C_{DG}(v_u - v_c)|\boldsymbol{v}_u - \boldsymbol{v}_c|^{J-1}$

56. $S_{x_u} = \alpha_u[g^x - \frac{\frac{1}{2}P_{b_u} h}{\alpha_u}\frac{\partial \alpha_c}{\partial x} + P_{b_u}\frac{\partial b}{\partial x} - \frac{\mathcal{A}\eta_u}{\alpha_u}(2\frac{\partial^2 u_u}{\partial x^2} + \frac{\partial^2 v_u}{\partial xy} + \frac{\partial^2 u_u}{\partial y^2} - \frac{\mathrm{X} u_u}{\epsilon^2 h^2}) + \frac{\mathcal{A}\eta_u}{\alpha_u}(2\frac{\partial}{\partial x}(\frac{\partial}{\partial x}(u_u - u_c)) + \frac{\partial}{\partial y}(\frac{\partial \alpha_c}{\partial x}(v_u - v_c) + \frac{\partial \alpha_u}{\partial y}(u_u - u_c))) - \frac{\mathcal{A}\eta_u \zeta \alpha_s(1-f_{sc})(u_u - u_c)}{\alpha_u h^2} - \frac{g}{n^2}\frac{\mathrm{u_u}|\mathrm{u_u}|}{h^{\frac{4}{3}}}] - \frac{1}{\gamma_c}C_{DG}(u_u - u_c)|\overrightarrow{u_u} - \overrightarrow{u_c}|^{J-1}$

57. $S_{y_u} = \alpha_u[g^y - \frac{\frac{1}{2}P_{b_u} h}{\alpha_f}\frac{\partial \alpha_c}{\partial y} + P_{b_u}\frac{\partial b}{\partial y} - \frac{\mathcal{A}\eta_u}{\alpha_u}(2\frac{\partial^2 u_f}{\partial y^2} + \frac{\partial^2 v_f}{\partial xy} + \frac{\partial^2 u_f}{\partial x^2} - \frac{\mathrm{X} u_f}{\epsilon^2 h^2}) + \frac{\mathcal{A}\eta_u}{\alpha_c}(2\frac{\partial}{\partial y}(\frac{\partial}{\partial y}(v_u - v_c)) + \frac{\partial}{\partial x}(\frac{\partial \alpha_c}{\partial y}(u_u - u_c) + \frac{\partial \alpha_c}{\partial x}(v_u - v_c))) - \frac{\mathcal{A}\eta_u \zeta \alpha_s(1-f_{sc})(v_u - v_c)}{\alpha_u h^2} - \frac{g}{n^2}\frac{\mathbf{v_u}|\mathbf{u_u}|}{h^{\frac{4}{3}}}] - \frac{1}{\gamma_c}C_{DG}(v_u - v_c)|\overrightarrow{u_u} - \overrightarrow{u_c}|^{J-1}$

58. $P_{b_c} = -(1 - f_{sc})(1 - \gamma)\frac{(1-f_{sc})\alpha_s}{(1-f_{fc})\alpha_f} g^z h - f_{sc}(1 - \gamma)\frac{(f_{sc})\alpha_s}{(f_{fc})\alpha_f} g^z h$

59. $P_{b_u} = -g^z h$

60. $\gamma_c = \frac{\rho_u}{\rho_c}, \gamma = \frac{\rho_f}{\rho_s}$

61. $C_{DG} = \frac{f_{sc}\alpha_c\alpha_u(\rho_c - \rho_f)g}{U_{T,c}(\mathcal{G}(Re)) + S_p} + \frac{(1-f_{sc})\alpha_c\alpha_u(\rho_s - \rho_f)g}{U_{T,uc}(\mathcal{P}\mathcal{F}(Re_p) + (1-\mathcal{P})\mathcal{G}(Re)) + S_p}$

62. $S_p = (\frac{\mathcal{P}}{\alpha_c} + \frac{1-\mathcal{P}}{\alpha_u})\mathcal{K}$

63. $\mathcal{K} = |\alpha_c \boldsymbol{u}_c + \alpha_u \boldsymbol{u}_u|$

64. $F = \frac{\gamma}{180}(\frac{\alpha_f}{\alpha_s})^3 Re_P, \ G = \alpha_f^{M(Re_p)-1}, \ Re_p = \frac{\rho_f d U_t}{\eta_f}, \ N_R = \frac{\sqrt{gL}H\rho_f}{\alpha_f\eta_f}, \ N_{RA} = \frac{\sqrt{gL}H\rho_f}{A\eta_f}$

65. $C_{Vm} = (\frac{1}{2}(\frac{1+2\alpha_c}{\alpha_u}))$

66. $\hat{\sigma} = \sigma^{\alpha\gamma}\dot{\omega}^{\beta\gamma} + \sigma^{\gamma\beta}\dot{\omega}^{\alpha\gamma} + 2G\dot{e}^{\alpha\beta} + K\dot{\epsilon}^{\gamma\gamma}\delta^{\alpha\beta} - \dot{\lambda}[9K\sin\psi\,\delta^{\alpha\beta} + \frac{G}{\sqrt{J_2}}s^{\alpha\beta}]$

417   67. $\dot{\lambda} = \dfrac{3\alpha K \dot{\epsilon}^{\gamma\gamma} + \left(\frac{G}{\sqrt{J_2}}\right) s^{\alpha\beta} \dot{\epsilon}^{\alpha\beta}}{27\alpha_\phi K \sin\psi + G}$

418   68. $K = \dfrac{E}{3(1-2\nu)}, G = \dfrac{E}{2(1+\nu)}$

419   69. $\sigma^{\alpha\beta} = s^{\alpha\beta} + \frac{1}{3}\sigma^{\gamma\gamma}\delta^{\alpha\beta}$

420   70. $\dot{\epsilon}^{\alpha\beta} = \frac{1}{2}\left(\frac{\partial v^\alpha}{\partial x^\beta} - \frac{\partial v^\beta}{\partial x^\alpha}\right)$ $\dot{\omega}^{\alpha\beta} = \frac{1}{2}\left(\frac{\partial v^\alpha}{\partial x^\beta} - \frac{\partial v^\beta}{\partial x^\alpha}\right)$

421   71. $\alpha_\phi = \dfrac{\tan(\phi)}{\sqrt{9+12\tan^2\phi}}$ $k_c = \dfrac{3c}{\sqrt{9+12\tan^2\phi}}$

422 Where X is the shape factor for vertical shearing of the fluid (X ≈ 3 in Iverson & Denlinger, 2001), R is the
423 precipitation rate and I is the infiltration rate.
424
425   **Closing the equations**
426 Viscosity is estimated using the empirical expression from O'Brien and Julien (1985), which relates dynamic
427 viscosity to the solid concentration of the fluid (Equation 72).

428   72. $\eta = \alpha e^{\beta\alpha_s}$

429   Where α is the first viscosity parameter and β the second viscosity parameter.

430   Finally, the settling velocity of small (d < 100 μm) grains is estimated by Stokes equations for a
431 homogeneous sphere in water. For larger grains (> 1mm),the equation by Zanke (1977) is used (Equation 30).

432   73. $U_T = 10 \dfrac{\frac{\eta}{\rho_f}^2}{d} \left(\sqrt{1 + \dfrac{0.01\left(\frac{(\rho_s - \rho_f)}{\rho_f} g d^3\right)}{\frac{\eta}{\rho_f}}} - 1 \right)$

433   In which U_T is the settling (or terminal) velocity of a solid grain, η is the dynamic viscosity of the fluid,
434 ρ_f is the density of the fluid, ρ_s is the density of the solids, d is the grain diameter (m)
435
436   **1.4 Implementation in the Material Point Method numerical scheme**

437   Implementing the presented set of equations into a numerical scheme requires considerations of that
438 schemes limitations and strengths (Stomakhin et al., 2013). Fluid dynamics are almost exclusively solved using
439 an Eulerian finite element solution (Delestre et al., 2014; Bout et al., 2018). The diffusive advection part of such
440 scheme typically doesn't degrade the quality of modelling results. Solid material however is commonly
441 simulated with higher accuracy using an Lagrangian finite element method or discrete element method (Maurel
442 & Cumbescure, 2008; Stomakhin et al., 2013). Such schemes more easily allow for the material to maintain its
443 physical properties during movement. Additionally, advection in these schemes does not artificially diffuse the
444 material since the material itself is discretized, instead of the space (grid) on which the equations are solved. In
445 our case, the material point method (MPM) provides an appropriate tool to implement the set of presented
446 equations (Bui et al., 2008; Maurel & Cumbescure, 2008; Stomakhin et al., 2013). Numerous existing modelling
447 studies have implemented in this method (Pastor et al., 2007; Pastor et al., 2008; Abe & Kanogai, 2016). Here,
448 we use the MPM method to create a two-phase scheme. This allows the usage of finite elements aspects for the
449 fluid dynamics, which are so successfully described by the that method (particularly for water in larger areas, see
450 Bout et al., 2018).

451   **Mathematical Framework**

452   The mathematic framework of smooth-particles solves differential equations using discretized volumes
453 of mass represented by kernel functions (Libersky & Petschek, 1991; Bui et al., 2008; Stomakhin et al., 2013).
454 Here, we use the cubic spline kernel as used by Monaghan (2000) (Equation 74).

455   74. $W(r,h) = \begin{cases} \frac{10}{7\pi h^2}\left(1 - \frac{3}{2}q^2 + \frac{3}{4}q^3\right) & 0 \le |q| \ge 2 \\ \frac{10}{28\pi h^2}(2-q)^3 & 1 \le |q| < 2 \\ 0 & |q| \ge 2 \,|\, q < 0 \end{cases}$

456   Where r is the distance, h is the kernel size and q is the normalized distance ($q = \frac{r}{h}$)

$W(x)$, Kernel Function

h

Integration domain
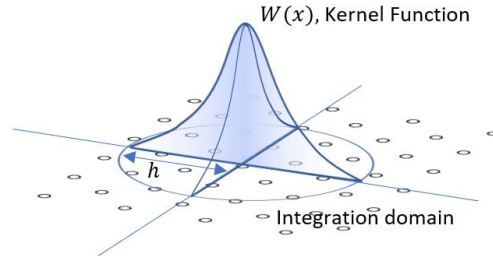
457

458   *Figure 2 Example of a kernel function used as integration domain for mathematical operations.*

459   Using this function mathematical operators can be defined. The average is calculated using a weighted
460   sum of particle values (Equation 75) while the derivative depends on the function values and the derivative of
461   the kernel by means of the chain rule (Equation 76) (Libersky & Petschek, 1991; Bui et al., 2008).

462   75. $\langle f(x) \rangle = \sum_{j=1}^{N} \frac{m_j}{\rho_j} f(x_j) W(x - x_j, h)$

463   76. $\langle \frac{\partial f(x)}{\partial x} \rangle = \sum_{j=1}^{N} \frac{m_j}{\rho_j} f(x_j) \frac{\partial W_{ij}}{\partial x_i}$

464   Where $W_{ij} = W(x_i - x_j, h)$ is the weight of particle j to particle I, $r = |x_i - x_j|$ is the distance
465   between two particles. The derivative of the weight function is defined by equation 77.

466   77. $\frac{\partial W_{ij}}{\partial x_i} = \frac{x_i - x_j}{r} \frac{\partial W_{ij}}{\partial r}$

467   Using these tools, the momentum equations for the particles can be defined (Equations 78-84). Here, we
468   follow Monaghan (1999) and Bui et al. (2008) for the definition of artificial numerical forces related to stability.
469   Additionally, stress-based forces are calculated on the particle level, while other momentum source terms are
470   solved on a Eulerian grid with spacing h (identical to the kernel size).

471   78. $\frac{dv_i^\alpha}{dt} = \frac{1}{m_i}(F_g + F_{grid}) + \sum_{j=1}^{N} m_j \left(\frac{\sigma_i^{\alpha\beta}}{\rho_i^2} + \frac{\sigma_j^{\alpha\beta}}{\rho_j^2} + F_{ij}^n R_{ij}^{\alpha\beta} + \Pi_{ij}\delta^{\alpha\beta} \right) \frac{\partial W_{ij}}{\partial x_i^\beta}$

472   79. $\dot\epsilon^{\alpha\beta} = \frac{1}{2} \left(\sum_{j=1}^{N} \frac{m_j}{\rho_j} (v_j^\alpha - v_i^\alpha) \frac{\partial W_{ij}}{\partial x_i^\beta} + \sum_{j=1}^{N} \frac{m_j}{\rho_j} (v_j^\beta - v_i^\beta) \frac{\partial W_{ij}}{\partial x_i^\alpha} \right)$

473   80. $\dot\omega^{\alpha\beta} = \frac{1}{2} \left(\sum_{j=1}^{N} \frac{m_j}{\rho_j} (v_j^\alpha - v_i^\alpha) \frac{\partial W_{ij}}{\partial x_i^\beta} - \sum_{j=1}^{N} \frac{m_j}{\rho_j} (v_j^\beta - v_i^\beta) \frac{\partial W_{ij}}{\partial x_i^\alpha} \right)$

474   81. $\frac{d\sigma_{\alpha\beta}}{dt} = \sigma_i^{\alpha\gamma} \dot\omega_i^{\beta\gamma} + \sigma_i^{\gamma\beta} \dot\omega_i^{\alpha\gamma} + 2G_i \dot e_i^{\alpha\beta} + K_i \dot\epsilon^{\gamma\gamma} \delta_i^{\alpha\beta} - \dot\lambda_\iota \left[9K_i sin\psi_i \, \delta^{\alpha\beta} + \frac{G_i}{\sqrt{J_{2i}}} s_i^{\alpha\beta} \right]$

475   82. $\dot\lambda_\iota = \frac{3\alpha K \dot\epsilon_i^{\gamma\gamma} + \left(\frac{G_i}{\sqrt{J_{2i}}} \right) s_i^{\alpha\beta} \dot\epsilon_\iota^{\alpha\beta}}{27\alpha_\phi K_i sin\psi_i + G_i}$

476   Where i, j are indices indicating the particle, Π_{ij} is an artificial viscous force as defined by equations 83
477   and 84 and $F_{ij}^n R_{ij}^{\alpha\beta}$ is an artificial stress term as defined by equations 85 and 86.

478   83. $\Pi_{ij} = \begin{cases} \frac{\alpha_\Pi u_{sound_{ij}} \phi_{ij} + \beta_\Pi \phi^2}{\rho_{ij}} & v_{ij} \cdot x_{ij} < 0 \\ 0 & v_{ij} \cdot x_{ij} \geq 0 \end{cases}$

479   84. $\phi_{ij} = \frac{h_{ij} v_{ij} x_{ij}}{|x_{ij}|^2 + 0.01 h_{ij}^2}$, $x_{ij} = x_i - x_j$, $v_{ij} = v_i - v_j$, $h_{ij} = \frac{1}{2}(h_i + h_j)$

480   85. $F_{ij}^n R_{ij}^{\alpha\beta} = \left[\frac{W_{ij}}{W(d_0, h)} \right]^n (R_i^{\alpha\beta} + R_j^{\alpha\beta})$

481   86. $\overline{R_\iota^{\gamma\gamma}} = -\frac{\epsilon_0 \overline{\sigma_\iota^{\gamma\gamma}}}{\rho_i^2}$

482   Where ϵ_0 is a small parameter ranging from 0 to 1, α_Π and β_Π are constants in the artificial viscous
483   force (often chosen close to 1), u_{sound} is the speed of sound in the material.

484   The conversion from particles to gridded values and reversed depends on a grid basis function that
485 weighs the influence of particle values for a grid center. Here, a function derived from dyadic products of one-
486 dimensional cubic B-splines is used as was done by Steffen et al. (2008) and Stomakhin et al. (2013) (Equation
487 84).

488   87. $N(x) = N(x^x) * N(x^y), \quad N(x) = \begin{cases} \frac{1}{2}|x|^3 - x^2 + \frac{2}{3} & 0 \le |x| \ge 2 \\ -\frac{1}{6}|x|^3 + x^2 - 2|x| + \frac{4}{3} & 1 \le |x| < 2 \\ 0 & |x| \ge 2 \mid x = 0 \end{cases}$

489   **Particle placement**

490   Particle placement is typically done in a constant pattern, as initial conditions have some constant
491 density. The simplest approach is a regular square or triangular network, with particles on the corners of the
492 network. Here, we use an approach that is more adaptable to spatially-varying initial flow height. The R_2
493 sequence approaches, with a regular quasirandom sequence, a set of evenly distributed points within a square
494 (Roberts, 2020) (Equation 85).

495   88. $x_n = n\alpha \bmod 1, \quad \alpha = \left(\frac{1}{c_p}, \frac{1}{c_p^2}\right)$

496   Where x_n is the relative location of the nth particle within a gridcell, $c_p = \left(\frac{9+\sqrt{69}}{18}\right)^{\frac{1}{3}} + \left(\frac{9-\sqrt{69}}{18}\right)^{\frac{1}{3}} \approx$
497 1.32471795572 is the plastic constant.
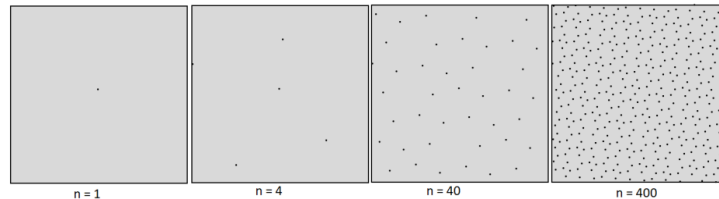
498
499   *Figure 3 Example particle distributions using the R_2 sequence, note that, while not all particles are*
500   *equidistant, the method produces distributed particle patterns that adapt well to varying density.*

501   The number of particles placed for a particular flow height depends on the particle volume V_l, which is
502 taken as a global constant during the simulation.

2   Flume Experiments
2.1 Flume Setup

505   In order to validate the presented model, several controlled experiments were performed and reproduced
506 using the developed equations. The flume setup consists of a steep incline, followed by a near-flat runout plane
507 (Figure 3). On the separation point of the two planes, a massive and attached obstacle is present that blocks the
508 path of two fifth of the moving material. For the exact dimensions of both the flume parts and the obstacle, see
509 figure 3.
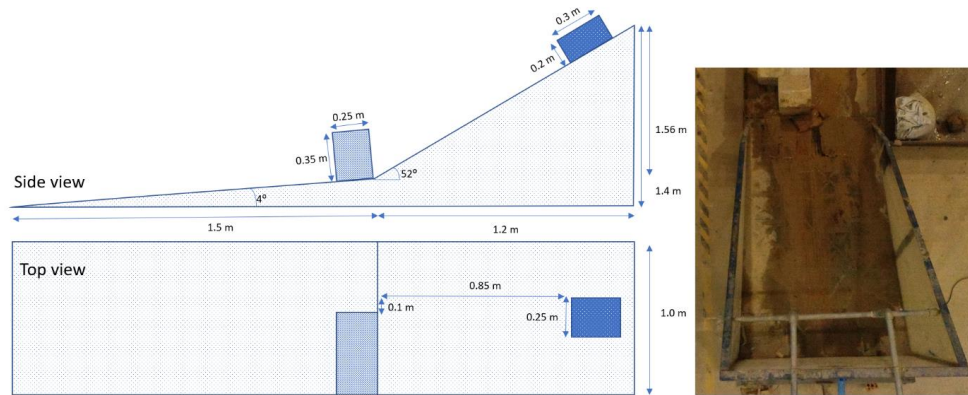
510
511 *Figure 4 The dimensions of the flume experiment setup used in this work.*

512   Two tests were performed whereby a cohesive granular matrix was released at the upper part of the
513 flume setup. Both of these volumes had dimensions of 0.2x0.3x0.25 meter (height,length,width). For both of
514 these materials, a mixture high-organic content silty-clay soils where used. The materials strength parameters
515 were obtained using tri-axial testing (Cohesion, internal friction angle Youngs modulus and Poisson Ration. The
516 first set of materials properties where $c = 26.7$ kPa and $\phi = 28°$. The second set materials properties where $c =$
517 18.3 kPa and $\phi = 27°$. For both of the events, pre-and post release elevations models were made using
518 photogrammetry. The model was set up to replicate the situations using the measured input parameters.
519 Numerical settings were chosen as $\{\alpha_s = 0.5, \alpha_f = 0.5, f_{sc} = 1.0, f_{fc} = 1.0, \rho_f = 1000, \rho_s = 2400, E = 12 \cdot$
520 $10^6 \, Pa, K = 23 \cdot 10^6 \, Pa, \psi = 0, \alpha_\Pi = 1, \beta_\Pi = 1, X, \zeta, j = 2, u_{sound} = 600, dx = 10, V_l =, h = 10, n =$
521 $0.1, \alpha = 1, \beta = 10, M = 2.4, \mathcal{B} = 0, N_R = 15000, N_{RA} = 30\}$. Calibration was performed by means of input
522 variation. The solid fraction, and elastic and bulk modulus were varied between 20 and 200 percent of their
523 original values with increments of 10 percent. Accuracy was assessed based on the percentage accuracy of the
524 deposition (comparison of modelled vs observed presence of material).

525 **2.2 Results**

526   Both the mapped extent of the material after flume experiments, as the simulation results are shown in
527 figure 5. Calibrated values for the simulations are $\{\alpha_s = 0.45, E = 21.6 \cdot 10^6 \, Pa, K = 13.8 \cdot 10^6 \, Pa\}$.

14
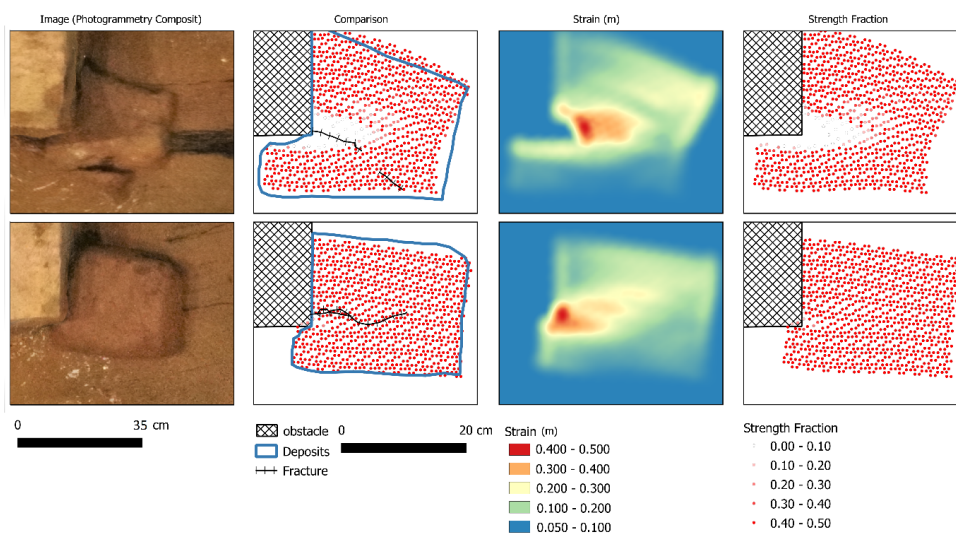
Figure 5 A comparison of the final deposits of the simulations and the mapped final deposits and cracks within the material. From left to right: Photogrammetry mosaic, comparison of simulation results to mapped flume experiment, strain, final strength fraction remaining.

As soon as the block of material impacts the obstacle, stress increases as the moving objects is deformed. This stress quickly propagates through the object. Within the scenario with lower cohesive strength, as soon as the stress reached beyond the yield strength, degradation of strength parameters took place. In the results, a fracture line developed along the corner of the obstacle into the length direction of the moving mass. Eventually, this fracture developed to half the length of the moving body and severe deformation resulted. As was observed from the tests, the first material experienced a critical fracture while the second test resulted in moderate deformation near the impact location. Generally, the results compare well with the observed patters, although the exact shape of the fracture is not replicated. Several reasons might be the cause of the moderately accurate fracture patterns. Other studies used a more controlled setup where uncertainties in applied stress and material properties where reduced. Furthermore, the homogeneity of the material used in the tests can not completely assumed. Realistically, minor alterations in compression used to create the clay blocks has left spatial variation in density, cohesion and other strength parameters.
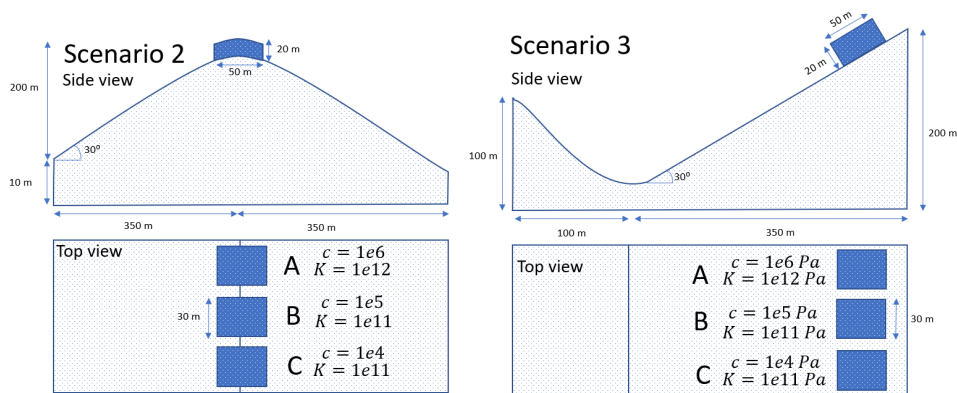
3. Numerical Tests

3.1 Numerical Setup

In order to further investigate some of the behaviors of the model, and highlight the novel types of mass movement dynamics that the model implements, several numerical tests have been performed. The setup of these tests is shown in figure 6.

Geoscientific
Model Development
Discussions

549

550
551 *Figure 6 The dimensions of the numerical experiment setups used in this work. Setup 1 (left) and Setup 2 (right)*

552   Numerical settings were chosen for three different blocks with equal volume but distinct properties.
553 Cohesive strength and the bulk modulus were varied (see figure 6). Remaining parameters were chosen as
554 $\{\alpha_s = 0.5, \alpha_f = 0.5, f_{sc} = 1.0, f_{fc} = 1.0, \rho_f = 1000\ kgm^{-3}, \rho_s = 2400\ kgm^{-3}, E = 1e12\ Pa, \psi = 0, \alpha_\Pi =$
555 $1, \beta_\Pi = 1, X, \zeta, j = 2, u_{sound} = 600\ ms^{-1}, dx = 10\ m, V_I, h = 10\ m, n = 0.1, \alpha = 1, \beta = 10, M = 2.4, \mathcal{B} =$
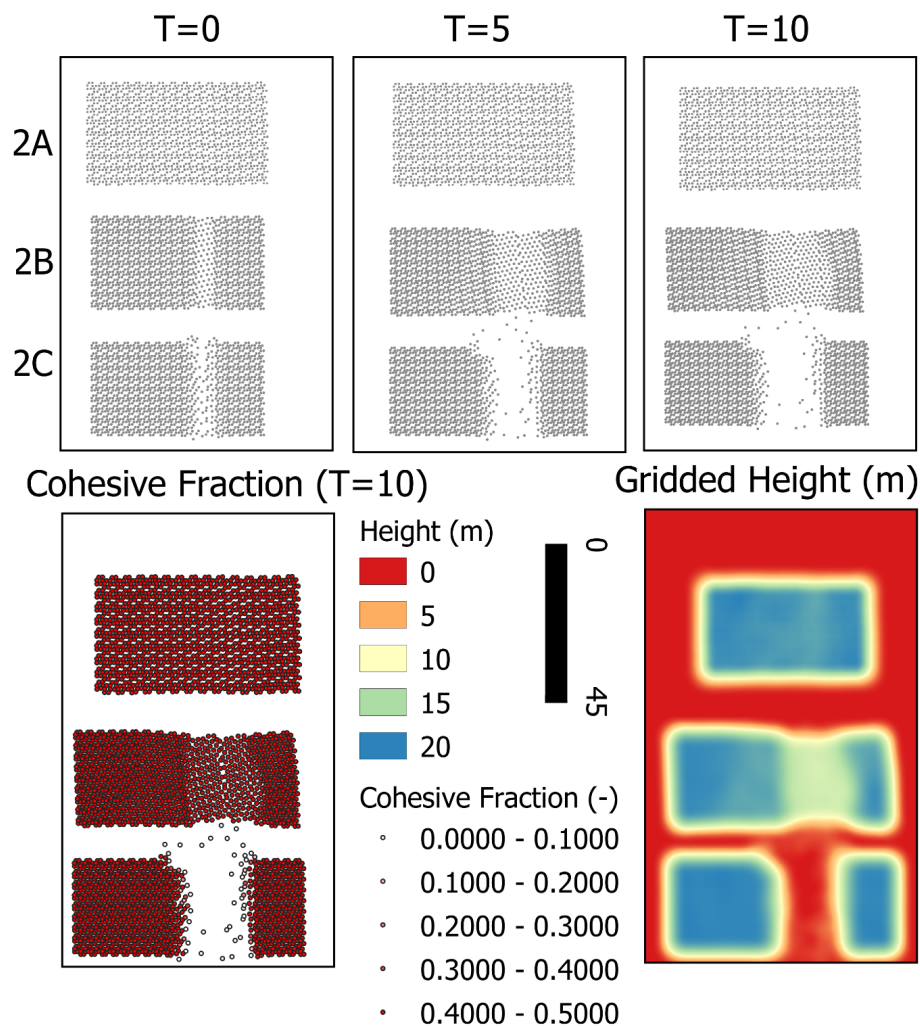556 $0, N_R = 15000, N_{RA} = 30\}.$

557   **3.1 Results**

558   Several time-slices for the described numerical scenarios are shown in figure 7 and 8.
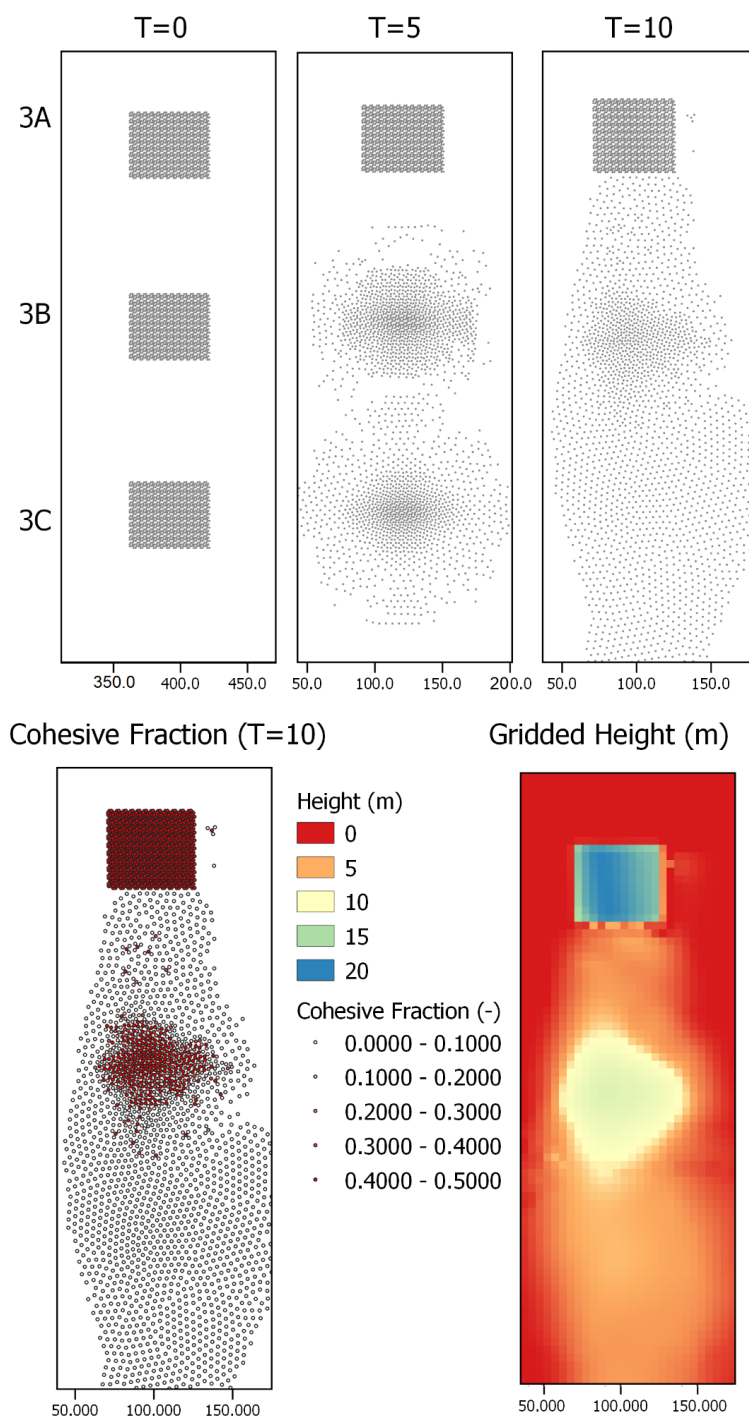
559

560

561   *Figure 7 Several time-slices for numerical scenarios 2(A/B/C). See figure 6 for the dimensions and*
562   *terrain setup.*

563
564   *Figure 8 Several time-slices for numerical scenarios 3(A/B/C). See figure 6 for the dimensions and terrain setup.*

18

565 Fractures develop in the mass movements based on acceleration differences and cohesive strength. For
566 scenario 2A, the stress state does not reach beyond the yield surface, and all material is moved as a single block.
567 Scenario 2B, which features lowered cohesive strength, fractures and the masses separate based on the
568 acceleration caused by slopes.

569 Fracturing behavior can occur in MPM schemes due to numerical limitations inherent in the usage of a
570 limited integration domain. Here, validation of real physically-based fracturing is present in the remaining
571 cohesive fraction. This value only reduces in case of plastic yield, where increasing strain degrades strength
572 parameters according to our proposed criteria. Numerical fractures would thus have a cohesive fraction of 1. In
573 all simulated scenarios, such numerical issues were not observed.

574 Fragmentation occurs due to spatial variation in acceleration in the case of scenario 3A and 3B. For
575 scenario 3A, the yield surface is not reached and the original structure of the mass is maintained during
576 movement. For 3C, fragmentation is induced be lateral pressure and buoyancy forces alone. Scenario 3B
577 experiences slight fragmentation at the edges of the mass, but predominantly fragments when reaching the
578 valley, after which part of the material is accelerated to count to the velocity of the mass. For all the shown
579 simulations, fragmentation does not lead to significant phase separation since virtual mass and drag forces
580 converge the separate phase velocities to their mixture-averaged velocity. The strength of these forces partly
581 depends on the parameters, effects of more immediate phase-separation could by studied if other parameters are
582 used as input.

583 **4. Discussion**

584 A variety of existing landslide models simulate the behavior of lateral connected material through a
585 non-linear, non-Newtonian viscous relationship (Boetticher et al., 2016; Fornes et al., 2017; Pudasaini &
586 Mergili, 2019). These relationships include a yield stress and are usually regularized to prevent singularities from
587 occurring. While this approach is incredibly powerful, it is fundamentally different from the work proposed here.
588 These viscous approaches do not distinguish between elastic or plastic deformation, and typically ignore
589 deformations if stress is insufficient. Additionally, fracturing is not implemented in these models. The approach
590 taken in this work attempts to simulate a full stress-strain relationship with Mohr-Coulomb type yield surface.
591 This does provides new types of behavior and can be combined with non-Newtonian viscous approaches as
592 mentioned above. A major downside to the presented work is the steep increase in computational time required
593 to maintain an accurate and stable simulation. Commonly, an increase of near a 100 times has been observed
594 during the development of the presented model.

595 The presented model shows a good likeness to flume experiments and numerical tests highlight
596 behavior that is commonly observed for landslide movements. There are however, inherent scaling issues and the
597 material used in the flume experiments is unlikely to form larger landslide masses. The measured physical
598 strength parameters of the material used in the flume experiments would not allow for sustained structured
599 movement at larger scales. There is thus the need for more, real-scale, validation cases. The application of the
600 presented type of model is most directly noticeable for block-type landslide movements that have fragmented
601 either upon impact of some obstacle or during transition phase. Of importance here is that the moment of
602 fragmentation is often not reported in studies on fast-moving landslides, potentially due to the complexities in
603 knowing the details on this behavior from post-event evidence. Validation would therefore have to occur on
604 cases where deposits are not fully fragmented, indicating that this process was ongoing during the whole
605 movement duration. The spatial extent of initiation and deposition would then allow validation of the model.
606 Another major opportunity for validation of the novel aspects of the model is the full three-dimensional
607 application to landslides that were reported to have lubrication effects due to fragmentation of lower fraction of
608 flow due to shear.

609 An important point of consideration in the development of complex multi-process generalized models is
610 the applicability. As a detailed investigative research tool, these models provide a basic scenario of usage.
611 However, both for research and beyond this, in applicability in disaster risk reduction decision support, the
612 benefit drawn from these models depends on the practical requirement for parameterization and the
613 computational demands for simulation. With an increasing complexity in the description of multi-process
614 mechanics comes the requirement of more measured or estimated physical parameters. Inspection of the
615 presented method shows that in principle, a minor amount of new parameters are introduced. The cohesive
616 strength, a major focus of the model, becomes highly important depending on the type of movement being
617 investigated. Additionally, the bulk and elastic modulus are required. These three parameters are common
618 simulation parameters in geotechnical research and can be obtained from common tests on sampled material
619 (Alsalman et al., 2015). Finally, the basal pressure propagation parameter ($\mathcal{B}$) is introduced. However, within
620 this work, the value of this parameter is chosen to have a constant value of one. As a results, the model does
621 require additional parameters, although these are relatively easy to obtain with accuracy.

19

622   There are a variety of aspects of the model that could be significantly improved. Here, we list several
623 major opportunities of future research.

1) **Groundwater mechanics**

625   The presented model allows for the a solid or granular matrix to be present within the flow. We have
626   assumed the flows in and out of these matrices are sufficiently small to be ignored. In reality, there is a
627   fluid flux in and out of structured solids. This could occur both due to pressure differences as due to
628   stress and strain of the structured solids. Implementing this kind of mechanics requires a dynamic,
629   solid-properties dependent, soil water retention curve (Van Looy et al., 2017). An example of MPM soil
630   mechanics with dynamic groundwater implementation can be found in Bandera et al. (2016).

2) **Implementing Entrainment and Deposition**

632   Current equations for entrainment (erosion with major grain-grain interactions) is limited to
633   unstructured mixture flows (Iverson, 2012; Iverson & Ouyang, 2015; Pudasaini & Fischer, 2016).
634   Extending these models to include a contribution from structured solids would be required to implement
635   entrainment in the presented work.

3) **Separation of phases**

637   A major assumption in the presented work is that the velocities of structured solids, free solids and
638   confined fluids are all equal. In reality, there might be separation of structured and free solids phases.
639   Additionally, we already discussed the possibility of in-and outflux of confined fluids from the solid
640   matrix. Recent innovations on three-phase mixture flows might be used to extend the presented work to
641   a three, four or five-phase model by separating free solids, confined fluids or adding a Bingham-viscous
642   solid-fluid phase (Pudasaini & Mergili, 2019). However, while this would implement an additional
643   process, it would significantly increase complexity of the equations (in an exponential manner with
644   relation to the number of phases) and the numerical solutions which could hinder practical applicability.

4) **Application to large, slow moving landslides.**

646   When confined fluids would act as a distinct phase, guided by the mechanics of water flow in granular
647   matrix, ground water pressures and movement through the structured solids could be described. This
648   might enable the model to do detailed deformation/groundwater simulation of large slow-moving
649   landslides.

5) **Numerical Improvements**

651   Numerical techniques for particle-based discretized methods (SPH, MPM) have been proposed in the
652   literature. A common issue is numerical fracturing of materials when particle strain increases beyond
653   the length of the kernel function. Then, the connection between particles is lost and fracturing occurs as
654   an artifact of the numerical method. This issue is partly solved by the artificial stress term as is also
655   used by Bui et al. (2008). Additionally, geometric subdivide, as used by Xu et al. (2012) and Li et al.
656   (2015), could counter these artificial fractures. Implementing this technique does require additional
657   work to maintain mass and momentum conservation.

6) **Three-dimensional solutions**

659   In a variety of scenarios, the assumptions made in depth-averaged application of flow models are
660   invalid. A common example is the impact of mass movements into lakes, or other large water bodies. In
661   such cases, the vertical velocity and concentration variables are not well-described by their depth-
662   averaged counterparts. Additionally, the lubrication effect of basal fragmentation of landslides due to
663   shear can not be described without velocity-profiles and a vertical stress-solution. Full three-
664   dimensional application would therefore have the potential to increase understanding on these important
665   processes.

5. Conclusions

667   We have presented a novel generalized mass movement model that can describe both unstructured
668 mixture flows and Structured movements of Mohr-Coulomb type material. The presented equations are part of
669 the continuous development of the OpenLISEM Hazard model, an open-source tool for physically-based multi-
670 hazard simulations. The model builds on the works of Pudasaini (2012) and Bui et al. (2008) to develop a single
671 holistic set of equations. The model was implemented in a GPU-based Material Point Method (MPM) Code. The
672 equations were validated on flume experiments and numerical tests, that highlight the new movement dynamics
673 possible with the presented model. The integration of cohesive structure and a full stress-strain relationship for
674 the structured solids allows for movement of block-type slides as a single whole. Interactions with terrain, other
675 flow masses or obstacles lead to elastic-plastic deformation and eventually fragmentation. This type of self-
676 alteration of flow properties is novel with mass movement models. Although the presented equations can provide
677 additional detail for specific mass movement types, applicability of the model for real events need to be
678 investigated as computational costs are significantly increased.

679   The presented simulation both validate the basic behavior of the model, as well as highlight the types of
680 flow dynamics made possible by the presented equations. The models dependency of breaking to cohesive
681 strength and internal friction angle matches the flume experiments. The numerical examples show commonly-
682 described behavior for landslide movements. Although the simulations compare well to the flume experiments,
683 validation is required for real-scale application to various types of mass movements. Additionally, the presented
684 equations still lack descriptions of processes that might become important. Separating the fluid and solid phases
685 such as done by Pudasaini & Mergili (2019), could improve flow dynamics and phase separation. With added
686 ground-water mechanics, such as done in Bandera et al. (2016), slow-moving landslide simulations might be
687 described.

6. Code and Data Availability

689   All code and data used within this work are made open-source as part of the continuous development of
690 the OpenLISEM Hazard model under the GNU General Public Licence v3.0. The code and the data are hosted
691 on Github (https://github.com/bastianvandenbout/OpenLISEM-Hazard-2.0-Pre-Release). Both binaries
692 and a copy of the source code are also available on Sourceforge, where the manual and compilation guide can
693 similarly be found (https://sourceforge.net/projects/lisem/). Finally, more information can be found at the blog
694 (https://blog.utwente.nl/lisem/)

695   The software, and its user interface, are written for windows, but platform independent libraries are
696 used and compilation might be performed on other platforms.
697 Hardware requirements for the usage of the model are a 64-bit Operating system that can compile all required
698 external libraries (see the manual for a full list and description). A graphical processing unit conforming to at
699 least the OpenCL 1.2 standard and support for both OpenGL 4.2 and OpenGL/OpenCL interoperability.
700 Additionally, an approximate 500 mb of hard drive space and 750 mb of memory must be available.

701

Appendix A. List of Symbols

702

703   h is the flow height

704 s is the solid phase

705 f is the fluid phase

706 sc is the structured solid phase

707 fc is the confined fluid phase

708 ρ_f is the density of fluids

709 ρ_s is the density of solids

710 α_f is the volumetric fluid phase fraction

711 α_s is the volumetric solid phase fraction

712 f_{sc} is the fraction of solids that is structured (confining)

713 f_{fc} is the fraction of fluids that is confined

714 α_c is the volumetric fraction of solids, structured solids and confined fluids

715 α_u is the volumetric fraction of free fluids (unconfined phase).

716 ρ_{sc} is the volume-averaged density of the solids and confined fluids

717 $\boldsymbol{u_u}$ is the velocity of the unconfined phase (free fluids)

718 $\boldsymbol{u_c}$ is the velocity of the solids, confining solids and confined fluids

719 $\boldsymbol{u_s}$ is the velocity of the solids

720 $\boldsymbol{f}$ is the body force

721 $\boldsymbol{M_{DG}}$ is the drag force

722 $\boldsymbol{M_{vm}}$ is the virtual mass force

723 $\boldsymbol{T_c}$ is the stress tensor for eh solids, confining solids and confined fluids

724 $\boldsymbol{T_u}$ is the stress tensor for the free fluid phase

725 $\boldsymbol{\sigma}$ is the stress tensor

726 $\dot{s}$ is the deviatoric shear stress rate tensor

727 δ is the Kronecker delta

728 $\dot{\epsilon}_{plastic}$ is the plastic strain rate

729 $\dot{\epsilon}_{elastic}$ is the elastic strain rate

730 λ is the plastic multiplier rate

731 g is the plastic potential function

732 $\dot{\epsilon}_{total}$ is the total strain rate

733 $\dot{e}$ is the deviatoric strain rate

734 ν is Poisson's ratio

735 E is the elastic Young's Modulus

736 G is the shear modulus

737 K is the Bulk elastic modulus

738 $f(I_1, J_2)$ is the yield surface, or yield criterion

739 $g(I_1, J_2)$ is the plastic potential function

740 ψ is the dilatancy angle

741 I_1 is the first stress invariant

742 J_2 is the second stress invariant

743 α_ϕ is the first Ducker-Prager material constant

744 k_c is the second Ducker-Prager material constant

745 $\dot{\omega}$ is the spin rate tensor

746 ϵ_{v0} is the initial volumetric strain

747 ϵ_v is the volumetric strain

748 c_0 is the initial cohesion

749 $\boldsymbol{\tau_f}$ is the fluid Gauchy stress tensor

750 P_f is the fluid pressure

751 η_f is the fluids dynamic viscosity

752 $\mathcal{A}$ is the mobility of the fluid at the interface

753 $\mathcal{C}_{DG}$ is the drag coefficient

754 $U_{T,c}$ is the settling velocity of the solids, structured solids and confined fluids

755 $U_{T,uc}$ is the settling velocity of the unstructured solids

756 $\mathcal{F}$ is the drag contribution from solid-like drag

757 $\mathcal{G}$ is the drag contribution from fluid-like drag

758 S_p is the smoothing function

759 $\mathcal{K}$ is the absolute total mass flux

760   $M(Re_p)$ is an empirical function weakly dependent on the Reynolds number
761   $\mathcal{P}$ the partitioning parameter for the fluid and solid like contributions to drag
762   m is an exponent for $\mathcal{P}$
763   $\mathcal{C}_{VMG}$ is the virtual mass coefficient
764   $|\boldsymbol{S}|$ is the norm of the shear force
765   N is the normal force on a plane element
766   g is the gravitational acceleration
767   $P_{b_{s,u}}$ is the basal pressure from
768   P_{b_u} is the basal pressure from the free fluids
769   P_{b_c} is the basal pressure from the solids, structured solids and confined fluids
770   $\mathcal{B}$ is the pressure propagation factor for structured solids
771   K_a is the active lateral earth pressure coefficient
772   K_p is the passive lateral earth pressure coefficient
773   ζ is a shape factor for the vertical gradient in solid concentration
774   n is Mannings surface roughness coefficient
775   X is the shape factor for the vertical fluid velocity profile
776   Re_p is the particle Reynolds Number
777   N_R is the Reynolds Number
778   N_{RA} is the interfacial Reynolds Number
779   H is the typical height of the flow
780   L is the typical length of the flow
781   α is the first viscosity parameter
782   β the second viscosity parameter
783   d is the grain diameter
784   W is the kernel weight function
785   r is the distance
786   h is the kernel width (not to be confused with the flow height)
787   q is the normalized particle distance
788   Π_{ij} is an artificial viscosity term
789   $F_{ij}^{n} R_{ij}^{\alpha\beta}$ is an artificial stress term
790   ϵ_0 is a constant parameter for the artificial stress term
791   α_{Π} and β_{Π} are constants in the artificial viscous force
792   u_{sound} is the speed of sound in the material
793   $N(\boldsymbol{x})$ is the Grid-kernel function
794   c_p is the plastic coefficient
795
796

797
798
799

800

801

802

803   **Appendix B. Stress Remapping**

804   If, either due to degradation of strength parameters, or building numerical errors, the state of the stress
805   tensor lies beyond the yield surface, a correction must be applied. We implement the correction scheme used by
806   Bui et al. (2008). This scheme considers two primary ways in which the stress can have an undesired state:
807   Tension cracking, and imperfectly plastic stress.

808   **Tension Cracking**

809   In the case of tension cracking, the stress state has moved beyond the apex of the yield surface, as
810   described by Chen & Mizuno (1990). The employed solution in this case is to re-map the stress tensor along the
811   I_1 axis to be at this apex. The apex is provided by the yield function (Equation 89)

812   89. $-\alpha_\phi I_1 + k_c < 0$

813   To solve for this condition, the non-deviatoric stress state is increased (since $I_1 - \frac{k_c}{\alpha_\phi}$ is negative) to lie

814   perpendicular to the apex point on the I_1 axis (Equation).

815   90. $\widetilde{\sigma^{\gamma\gamma}} = rs^{\gamma\gamma} - \frac{1}{3}\left(I_1 - \frac{k_c}{\alpha_\phi}\right)$

816   **Imperfect Plastic Stress**

817   Imperfect plastic stress described the state where the stress tensor lies above the apex, but beyond the
818   yield criterion, thus have more stress than supported by the failure criteria that is set. This criteria is simply the
819   yield surface itself (Equation 91).

820   91. $-\alpha_\phi I_1 + k_c < \sqrt{J_2}$

821   For this state, re-mapping is done by scaling of the J_2 value (Equations 92, 93 and 94).

822   92. $r = \frac{-\alpha_\phi I_1 + k_c}{\sqrt{J_2}}$

823   93. $\widetilde{\sigma^{\gamma\gamma}} = rs^{\gamma\gamma} + \frac{1}{3}I_1$

824   94. $\widetilde{\sigma^{xy}} = rs^{xy}, \widetilde{\sigma^{xy}} = rs^{xz}, \widetilde{\sigma^{xy}} = rs^{yz}$

825

826

827

828 **Appendix C. Software Implementation**

829 The model presented in this article is part of the continued development of the OpenLISEM modelling
830 tools. The most recent set of equations of implemented in the open-source alpha version of OpenLISEM Hazard
831 2. Here, we describe the details of the implementation of the model into software.

832 **Hybrid MPM**

833 We utilize the MPM framework to be able to discretize part of the equations on a Eulerian regural grid,
834 and part of the equations on the Lagrangian particles. Our distinct take on this method is the representation of the
835 fluid phase completely as a finite element solution, while solids are simulated as discrete particle volumes. This
836 allows the model to use the major benefits that are present when depth-averaged fluid flow is simulated in a grid.
837 Both numerical efficiency, and high-accuracy coupling with hydrology are lacking in particle methods. For the
838 solid phase, non-dissapative advection, fracturing and stiffness is a major benefit of the MPM approach. Since
839 our model assumed confined fluids share their velocity with the solids, we advect the confined fluids as part of
840 the particles. Total fluid volume is then calculated from the free fluids in the finite element data, and the gridded
841 particle data. A flowchart of the software setup is provided in figure 6.
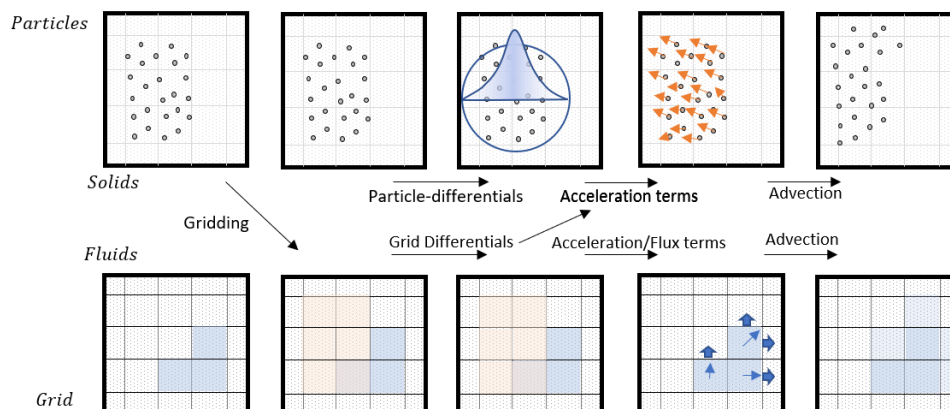
842
843 *Figure 9 The sub-steps taken by the software to complete a single step of numerical integration.*

844 **Finite element solution**

845 We use a regular cartesian grid to describe the modelling domain. Terrain and cell-boundary based
846 variables are re-produces using the MUSCL piecewise linear reconstruction (Delestre et al., 2014). For each cell-
847 boundary, a left and right estimation of acceleration terms, velocity updates and new discharges is made. The left
848 estimates use left-reconstructed variables while the other uses right-reconstructed variables. The final average
849 flux through the boundary determines actual mass and momentum transfer. Local acceleration is averaged from
850 the right estimate of the left boundary and left estimate of the right boundary. An additional benefit of the used
851 scheme is the automatic estimation of continuous and discontinuous terrain. The piecewise linear reconstructions
852 do not guarantee smooth terrain, for sharp locally variable terrain, pressure terms from vertical walls arise that
853 block momentum. These terms allow for better estimation of momentum loss by barriers, but can be turned off if
854 required for the simulated scenario.

855
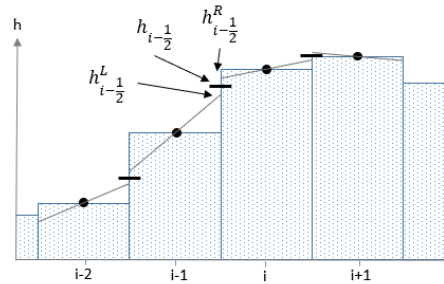
Figure 10 Piecewise linear reconstruction is used by the MUSCL scheme to estimate values of flow heights, velocities and terrain at cell-boundaries.

GPU acceleration using OpenCL/OpenGL

In order to create a more efficient setup, both the finite element and particle interactions are performed on the GPU. We utilize the OpenCL API to compile kernels written in c-style language. These kernels are compiled at the start of the simulation, and thereby allow for easy customization by users. While the usage of OpenCL 1.1 forces the usage of single precision floating point numbers, it allows for a wider range of GPU types to be supported. Finite element solutions on the GPU are straightforward, as maps are a basic data storage type for graphical processing units. Particles are stored as single-precision floating point arrays. Within the framework of MPM, iteration of particles within a kernel is required for each timestep and particle. This effectively means $O(n^2)$ operations are required. Significant efficiency improvements are obtained by pre-calculation sorting. Particles are sorted based on their location within the finite element grid. Based on the id of the gridcell, a bitonic mergesort is performed. This sorting algorithm works seamlessly on parallel architecture and operates as $O\left(nlog^2(n)\right)$ (Batcher, 1968). The then, a raster is allocated to store the first indexed occurrence within the sorted list of particles of that gridcell. Since the kernel used for the presented work extends at most to a full width of two gridcells, we must iterate over all particles present in 9 neighboring grid cells.

872
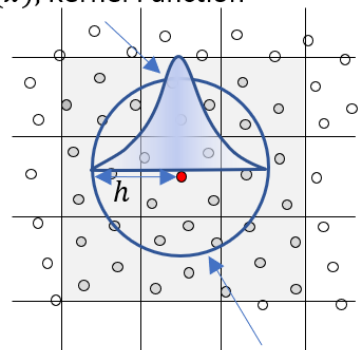
Figure 11 By limiting the kernel with and sorting particles before calculation, only the distance of particles in neighboring cells need to be checked, significantly reducing computational load, particularly for larger datasets.

A final benefit to the usage of OpenCL is direct access to simulation variables for visualization in OpenGL using the OpenGL/OpenCL interoperability functionality. The built-in viewing window of OpenLISEM Hazard 2.0 alpha directly uses the data to draw both particles, shapefiles and grid data using customizable shaders written in the openGL shader language.

881   **References**

882   Abe, K., & Konagai, K. (2016). Numerical simulation for runout process of debris flow using depth-
883   averaged material point method. *Soils and Foundations*, *56*(5), 869-888.

884   Alsalman, M. E., Myers, M. T., & Sharf-Aldin, M. H. (2015, November). Comparison of multistage to
885   single stage triaxial tests. In *49th US Rock Mechanics/Geomechanics Symposium*. American Rock Mechanics
886   Association.

887   Bandara, S., Ferrari, A., & Laloui, L. (2016). Modelling landslides in unsaturated slopes subjected to
888   rainfall infiltration using material point method. *International Journal for Numerical and Analytical Methods in
889   Geomechanics*, *40*(9), 1358-1380.

890   Batcher, K. E. (1968, April). Sorting networks and their applications. In *Proceedings of the April 30--
891   May 2, 1968, spring joint computer conference* (pp. 307-314).

892   Beutner, E. C., & Gerbi, G. P. (2005). Catastrophic emplacement of the Heart Mountain block slide,
893   Wyoming and Montana, USA. *Geological Society of America Bulletin*, *117*(5-6), 724-735.

894   Bieniawski, Z. T. (1967, October). Mechanism of brittle fracture of rock: part I—theory of the fracture
895   process. In *International Journal of Rock Mechanics and Mining Sciences & Geomechanics Abstracts* (Vol. 4,
896   No. 4, pp. 395-406). Pergamon.

897   Bout, B., & Jetten, V. G. (2018). The validity of flow approximations when simulating catchment-
898   integrated flash floods. *Journal of hydrology*, *556*, 674-688.

899   Bui, H. H., Fukagawa, R., Sako, K., & Ohno, S. (2008). Lagrangian meshfree particles method (SPH)
900   for large deformation and failure flows of geomaterial using elastic–plastic soil constitutive model. *International
901   journal for numerical and analytical methods in geomechanics*, *32*(12), 1537-1570.

902   Chen, W. F., & Mizuno, E. (1990). *Nonlinear analysis in soil mechanics* (No. BOOK). Amsterdam:
903   Elsevier.

904   Cohen, D., Lehmann, P., & Or, D. (2009). Fiber bundle model for multiscale modeling of
905   hydromechanical triggering of shallow landslides. *Water resources research*, *45*(10).

906   Corominas, J., Matas, G., & Ruiz-Carulla, R. (2019). Quantitative analysis of risk from fragmental
907   rockfalls. *Landslides*, *16*(1), 5-21.

908   Corominas, J., van Westen, C., Frattini, P., Cascini, L., Malet, J. P., Fotopoulou, S., ... & Pitilakis, K.
909   (2014). Recommendations for the quantitative analysis of landslide risk. *Bulletin of engineering geology and the
910   environment*, *73*(2), 209-263.

911   DAVID, L. G., & RICHARD, M. (2011). A two-phase debris-flow model that includes coupled
912   evolution of volume fractions, granular dilatancy, and pore-fluid pressure. *Italian journal of engineering geology
913   and Environment*, *43*, 415-424.

914   Davies, T. R., & McSaveney, M. J. (2009). The role of rock fragmentation in the motion of large
915   landslides. *Engineering Geology*, *109*(1-2), 67-79.

916   Davies, T. R., McSaveney, M. J., & Beetham, R. D. (2006). Rapid block glides: slide-surface
917   fragmentation in New Zealand's Waikaremoana landslide. *Quarterly Journal of Engineering Geology and
918   Hydrogeology*, *39*(2), 115-129.

919   De Vuyst, T., & Vignjevic, R. (2013). Total Lagrangian SPH modelling of necking and fracture in
920   electromagnetically driven rings. *International Journal of Fracture*, *180*(1), 53-70.

921   Delaney, K. B., & Evans, S. G. (2014). The 1997 Mount Munday landslide (British Columbia) and the
922   behaviour of rock avalanches on glacier surfaces. *Landslides*, *11*(6), 1019-1036.

923   Delestre, O., Cordier, S., Darboux, F., Du, M., James, F., Laguerre, C., ... & Planchon, O. (2014).
924   FullSWOF: A software for overland flow simulation. In *Advances in hydroinformatics* (pp. 221-231). Springer,
925   Singapore.

926   Dhanmeher, S. (2017). Crack pattern observations to finite element simulation: An exploratory study
927   for detailed assessment of reinforced concrete structures.

928   Drew, D. A. (1983). Mathematical modeling of two-phase flow. *Annual review of fluid
929   mechanics*, *15*(1), 261-291.

Dufresne, A., Geertsema, M., Shugar, D. H., Koppes, M., Higman, B., Haeussler, P. J., ... & Gulick, S. P. S. (2018). Sedimentology and geomorphology of a large tsunamigenic landslide, Taan Fiord, Alaska. *Sedimentary Geology*, *364*, 302-318.

Evans, S. G., Mugnozza, G. S., Strom, A. L., Hermanns, R. L., Ischuk, A., & Vinnichenko, S. (2006). Landslides from massive rock slope failure and associated phenomena. In *Landslides from massive rock slope failure* (pp. 03-52). Springer, Dordrecht.

Fornes, P., Bihs, H., Thakur, V. K. S., & Nordal, S. (2017). Implementation of non-Newtonian rheology for Debris Flow simulation with REEF3D. IAHR World Congress.

Grady, D. E., & Kipp, M. E. (1980, June). Continuum modelling of explosive fracture in oil shale. In *International Journal of Rock Mechanics and Mining Sciences & Geomechanics Abstracts* (Vol. 17, No. 3, pp. 147-157). Pergamon.

Griffiths, D. V., & Lane, P. A. (1999). Slope stability analysis by finite elements. *Geotechnique*, *49*(3), 387-403.

Hayir, A. (2003). The effects of variable speeds of a submarine block slide on near-field tsunami amplitudes. *Ocean engineering*, *30*(18), 2329-2342.

Hušek, M., Kala, J., Hokeš, F., & Král, P. (2016). Influence of SPH regularity and parameters in dynamic fracture phenomena. *Procedia engineering*, *161*, 489-496.

Hutter, K., Svendsen, B., & Rickenmann, D. (1994). Debris flow modeling: A review. *Continuum mechanics and thermodynamics*, *8*(1), 1-35.

Ishii, M. (1975). Thermo-fluid dynamic theory of two-phase flow. *NASA Sti/recon Technical Report A*, *75*.

Ishii, M., & Zuber, N. (1979). Drag coefficient and relative velocity in bubbly, droplet or particulate flows. *AIChE journal*, *25*(5), 843-855.

Iverson, R. M. (2012). Elementary theory of bed-sediment entrainment by debris flows and avalanches. *Journal of Geophysical Research: Earth Surface*, *117*(F3).

Iverson, R. M., & Denlinger, R. P. (2001). Flow of variably fluidized granular masses across three-dimensional terrain: 1. Coulomb mixture theory. *Journal of Geophysical Research: Solid Earth*, *106*(B1), 537-552.

Iverson, R. M., & Denlinger, R. P. (2001). Flow of variably fluidized granular masses across three-dimensional terrain: 1. Coulomb mixture theory. *Journal of Geophysical Research: Solid Earth*, *106*(B1), 537-552.

Iverson, R. M., & George, D. L. (2014). A depth-averaged debris-flow model that includes the effects of evolving dilatancy. I. Physical basis. *Proceedings of the Royal Society A: Mathematical, Physical and Engineering Sciences*, *470*(2170), 20130819.

Iverson, R. M., & Ouyang, C. (2015). Entrainment of bed material by Earth-surface mass flows: Review and reformulation of depth-integrated theory. *Reviews of Geophysics*, *53*(1), 27-58.

Jakob, M., Hungr, O., & Jakob, D. M. (2005). *Debris-flow hazards and related phenomena* (Vol. 739). Berlin: Springer.

Kaklauskas, G., & Ghaboussi, J. (2001). Stress-strain relations for cracked tensile concrete from RC beam tests. *Journal of Structural Engineering*, *127*(1), 64-73.

Kern, J. S. (1995). Evaluation of soil water retention models based on basic soil physical properties. *Soil Science Society of America Journal*, *59*(4), 1134-1141.

Kjekstad, O., & Highland, L. (2009). Economic and social impacts of landslides. In *Landslides–disaster risk reduction* (pp. 573-587). Springer, Berlin, Heidelberg.

Li, C., Wang, C., & Qin, H. (2015). Novel adaptive SPH with geometric subdivision for brittle fracture animation of anisotropic materials. *The Visual Computer*, *31*(6-8), 937-946.

Libersky, L. D., & Petschek, A. G. (1991). Smooth particle hydrodynamics with strength of materials. In *Advances in the free-Lagrange method including contributions on adaptive gridding and the smooth particle hydrodynamics method* (pp. 248-257). Springer, Berlin, Heidelberg.

979 Loehnert, S., & Mueller-Hoeppe, D. S. (2008). Multiscale methods for fracturing solids. In *IUTAM*
980 *symposium on theoretical, computational and modelling aspects of inelastic media* (pp. 79-87). Springer,
981 Dordrecht.

982 Luna, B. Q., Remaître, A., Van Asch, T. W., Malet, J. P., & Van Westen, C. J. (2012). Analysis of
983 debris flow behavior with a one dimensional run-out model incorporating entrainment. *Engineering*
984 *geology*, *128*, 63-75.

985 Ma, G. W., Wang, Q. S., Yi, X. W., & Wang, X. J. (2014). A modified SPH method for dynamic failure
986 simulation of heterogeneous material. *Mathematical Problems in Engineering*, *2014*.

987 Matsui, T., & San, K. C. (1992). Finite element slope stability analysis by shear strength reduction
988 technique. *Soils and foundations*, *32*(1), 59-70.

989 Maurel, B., & Combescure, A. (2008). An SPH shell formulation for plasticity and fracture analysis in
990 explicit dynamics. *International journal for numerical methods in engineering*, *76*(7), 949-971.

991 Menin, R. G., Trautwein, L. M., & Bittencourt, T. N. (2009). Smeared crack models for reinforced
992 concrete beams by finite element method. *RIEM-IBRACON Structures and Materials Journal*, *2*(2).

993 Monaghan, J. J. (2000). SPH without a tensile instability. *Journal of computational physics*, *159*(2),
994 290-311.

995 Nadim, F., Kjekstad, O., Peduzzi, P., Herold, C., & Jaedicke, C. (2006). Global landslide and avalanche
996 hotspots. *Landslides*, *3*(2), 159-173.

997 Necas, J., & Hlavácek, I. (2017). *Mathematical theory of elastic and elasto-plastic bodies: an*
998 *introduction*. Elsevier.

999 Ngekpe, B. E., Ode, T., & Eluozo, S. N. (2016). Application of total-strain crack model in finite
1000 element analysis for punching shear at edge connection. *International journal of Research in Engineering and*
1001 *Social Sciences*, *6*(12), 1-9.

1002 O'brien, J. S. (2007). FLO-2D users manual. *Nutr. Ariz. June*.

1003 O'brien, J. S., & Julien, P. Y. (1985). Physical properties and mechanics of hyperconcentrated sediment
1004 flows. *Proc. ASCE HD Delineation of landslides, flash flood and debris flow Hazards*.

1005 Osorno, M., & Steeb, H. (2017). Coupled SPH and Phase Field method for hydraulic
1006 fracturing. *PAMM*, *17*(1), 533-534.

1007 Pailha, M., & Pouliquen, O. (2009). A two-phase flow description of the initiation of underwater
1008 granular avalanches. *Journal of Fluid Mechanics*, *633*, 115-135.

1009 Pastor, M., Blanc, T., Haddad, B., Petrone, S., Morles, M. S., Drempetic, V., ... & Cuomo, S. (2014).
1010 Application of a SPH depth-integrated model to landslide run-out analysis. *Landslides*, *11*(5), 793-812.

1011 Pastor, M., Blanc, T., Pastor, M. J., Sanchez, M., Haddad, B., Mira, P., ... & Drempetic, V. (2007). A
1012 SPH depth integrated model with pore pressure coupling for fast landslides and related phenomena. In *2007*
1013 *international forum on landslides disaster management* (pp. 987-1014).

1014 Pastor, M., Haddad, B., Sorbino, G., Cuomo, S., & Drempetic, V. (2009). A depth-integrated, coupled
1015 SPH model for flow-like landslides and related phenomena. *International Journal for numerical and analytical*
1016 *methods in geomechanics*, *33*(2), 143-172.

1017 Pitman, E. B., & Le, L. (2005). A two-fluid model for avalanche and debris flows. *Philosophical*
1018 *Transactions of the Royal Society A: Mathematical, Physical and Engineering Sciences*, *363*(1832), 1573-1601.

1019 Price, N. J. (2016). *Fault and joint development: in brittle and semi-brittle rock*. Elsevier.

1020 Pudasaini, S. P. (2012). A general two-phase debris flow model. *Journal of Geophysical Research:*
1021 *Earth Surface*, *117*(F3).

1022 Pudasaini, S. P., & Fischer, J. T. (2016). A mechanical erosion model for two-phase mass flows. *arXiv*
1023 *preprint arXiv:1610.01806*.

1024 Pudasaini, S. P., & Hutter, K. (2003). Rapid shear flows of dry granular masses down curved and
1025 twisted channels. *Journal of Fluid Mechanics*, *495*, 193-208.

1026 Pudasaini, S. P., & Hutter, K. (2007). *Avalanche dynamics: dynamics of rapid flows of dense granular*
1027 *avalanches*. Springer Science & Business Media.

Geoscientific
Model Development
Discussions

1028   Pudasaini, S. P., & Mergili, M. (2019). A Multi-Phase Mass Flow Model. *Journal of Geophysical*
1029 *Research: Earth Surface*.

1030   Pudasaini, S. P., Hajra, S. G., Kandel, S., & Khattri, K. B. (2018). Analytical solutions to a nonlinear
1031 diffusion–advection equation. *Zeitschrift für angewandte Mathematik und Physik*, *69*(6), 150.

1032   Reiche, P. (1937). The Toreva-Block: A distinctive landslide type. *The Journal of Geology*, *45*(5), 538-
1033 548.Richard, A., Brennan, G., Oh, W. T., & Ileme, V. (2017). Critical height of an unsupported vertical trench in
1034 an unsaturated sand. In *Proceedings of the 70th Canadian Geotechnical Conference*.

1035   Rickenmann, D., Laigle, D. M. B. W., McArdell, B. W., & Hübl, J. (2006). Comparison of 2D debris-
1036 flow simulation models with field events. *Computational Geosciences*, *10*(2), 241-264.

1037   Roberts, M., http://extremelearning.com.au/evenly-distributing-points-in-a-triangle/ Obtained 29-01-
1038 2020

1039   Savage, S. B., & Hutter, K. (1989). The motion of a finite mass of granular material down a rough
1040 incline. *Journal of fluid mechanics*, *199*, 177-215.

1041   Saxton, K. E., & Rawls, W. J. (2006). Soil water characteristic estimates by texture and organic matter
1042 for hydrologic solutions. *Soil science society of America Journal*, *70*(5), 1569-1578.

1043   Sheridan, M. F., Stinton, A. J., Patra, A., Pitman, E. B., Bauer, A., & Nichita, C. C. (2005). Evaluating
1044 Titan2D mass-flow model using the 1963 Little Tahoma peak avalanches, Mount Rainier, Washington. *Journal*
1045 *of Volcanology and Geothermal Research*, *139*(1-2), 89-102.

1046   Stead, D., & Wolter, A. (2015). A critical review of rock slope failure mechanisms: The importance of
1047 structural geology. *Journal of Structural Geology*, *74*, 1-23.

1048   Steffen, M., Kirby, R. M., & Berzins, M. (2008). Analysis and reduction of quadrature errors in the
1049 material point method (MPM). *International journal for numerical methods in engineering*, *76*(6), 922-948.

1050   Sticko, S. (2013). Smooth Particle Hydrodynamics applied to fracture mechanics.

1051   Stomakhin, A., Schroeder, C., Chai, L., Teran, J., & Selle, A. (2013). A material point method for snow
1052 simulation. *ACM Transactions on Graphics (TOG)*, *32*(4), 1-10.

1053   Tang, C. L., Hu, J. C., Lin, M. L., Angelier, J., Lu, C. Y., Chan, Y. C., & Chu, H. T. (2009). The
1054 Tsaoling landslide triggered by the Chi-Chi earthquake, Taiwan: insights from a discrete element
1055 simulation. *Engineering Geology*, *106*(1-2), 1-19.

1056   Van Asch, T. W., Tang, C., Alkema, D., Zhu, J., & Zhou, W. (2014). An integrated model to assess
1057 critical rainfall thresholds for run-out distances of debris flows. *Natural hazards*, *70*(1), 299-311.

1058   Van Looy, K., Bouma, J., Herbst, M., Koestel, J., Minasny, B., Mishra, U., ... & Schaap, M. G. (2017).
1059 Pedotransfer functions in Earth system science: Challenges and perspectives. *Reviews of Geophysics*, *55*(4),
1060 1199-1256.

1061   Varnes, D. J. (1978). Slope movement types and processes. *Special report*, *176*, 11-33.

1062   von Boetticher, A., Turowski, J. M., McArdell, B. W., Rickenmann, D., & Kirchner, J. W. (2016).
1063 DebrisInterMixing-2.3: a finite volume solver for three-dimensional debris-flow simulations with two calibration
1064 parameters-Part 1: Model description. *Geoscientific Model Development*, *9*(9), 2909-2923.

1065   Williams, J. R. (2019, October). Application of SPH to coupled fluid-solid problems in the petroleum
1066 industry. In *Videos of Plenary Lectures presented at the IV International Conference on Particle-Based*
1067 *Methods. Fundamentals and Applications.(PARTICLES 2015)*.

1068   Xie, M., Esaki, T., & Cai, M. (2006). GIS-based implementation of three-dimensional limit equilibrium
1069 approach of slope stability. *Journal of geotechnical and geoenvironmental engineering*, *132*(5), 656-660.

1070   Xu, F., Zhao, Y., Li, Y., & Kikuchi, M. (2010). Study of numerical and physical fracture with SPH
1071 method. *Acta Mechanica Solida Sinica*, *23*(1), 49-56.

1072   Zhang, L. L., Zhang, J., Zhang, L. M., & Tang, W. H. (2011). Stability analysis of rainfall-induced
1073 slope failure: a review. *Proceedings of the Institution of Civil Engineers-Geotechnical Engineering*, *164*(5), 299-
1074 316.

1075   Zhou, F., Molinari, J. F., & Ramesh, K. T. (2005). A cohesive model based fragmentation analysis:
1076   effects of strain rate and initial defects distribution. *International Journal of Solids and Structures*, *42*(18-19),
1077   5181-5207.